

Year 2018–2019.

Program : M2-IMSES

Group : ISTO Geodynamics Team

Supervisor : Hugues Raimbourg and Stephane Scaillet.

# Deep metamorphic fluid circulation in the internal domains of the alpine chain. Ar isotopes and tracing of occluded fluids in the fluid inclusions of quartz

Melissa Bok Kharmujai KHARKONGOR

## Abstract

Subduction zones concentrate most of the flow of volatiles to the mantle. Dehydration reactions of minerals, and ascending fluid transfers, control the amounts of volatiles that are actually recycled to the mantle. To understand the fluid transfer in the deep parts of the subduction zones, it is necessary to go beyond the traditional isotopes (C, O, H) in order to explore other signatures allowing the tracing of fluids. These fluids are trapped in fluid inclusions within syn-tectonic veins, which constitutes therefore the best witness of the deep metamorphic aquifer. Based on this idea, we performed a preliminary work on quartz veins in the Alps oceanic domains (Flysch Helminthoid and Schistes Lustre) to understand how fluid composition varies with metamorphic grade. An experimental approach of in-situ UV laser ablation was applied to the quartz grains from the two different units in order to optimize the extraction and purification of Ar isotopes traces in the occluded fluids. The in-situ technique provides the control on texturally-tied fluid inclusion populations or fluid inclusion generations coexisting side by side at the scale of the fluid inclusion distribution. The results marked a variation isotopic composition from the different fluid inclusions present in the different textural setting. The  $^{40}\text{Ar}_{\text{tot}}/^{38}\text{Ar}_{\text{run}}$  vs  $^{40}\text{Ar}_{\text{tot}}/^{36}\text{Ar}_{\text{atm}}$  ratio is plotted to be able to have a comprehensive knowledge of the variation in the isotopic ratio. We have inferred that the fluid inclusions having an isotopic ratio which is non-atmospheric, have an exterior component that may have contributed to the difference in isotopic ratio. Differences in isotopic composition testify that temporal variations in fluid entrapment are associated with changes in fluid composition hence fluid source. However, the abundance of the  $^{39}\text{Ar}_K$  in all FI's is almost negligible indicating very low potassium concentration. This could provide an explanation of the apparent age calculated from the  $^{40}\text{Ar}/^{39}\text{Ar}$  data being unrealistically old ages with no geological significance, because the isotopic variations are dominated by the addition of unsupported  $^{40}\text{Ar}$  to the fluids. In this study, the correlation that has been made with the textural setting of fluid inclusions and their isotopic composition should be a great value for better understanding of the fluid circulation regime in the different structural units along the subduction plate.

Keywords: Fluid inclusions, Fluid circulation, Subduction, Schists lustre, Flysch Helminthoides

# Contents

1. Introduction	3
2. Geological Background	4
3. Analytical Technique	6
3.1 Sample Selection .....	6
3.2 Sample Preparation.....	6
3.3 Experimental Noble gas extraction technique.....	7
4. Petrographic Study of Samples	7
4.1 Flysh Helminthoides Samples.....	7
4.2 Schistes lustres Samples.....	8
5. Results	13
5.1 Flysh Helminthoides Samples.....	13
5.2 Schistes lustres Samples .....	16
6. Discussion	20
7. Conclusion	27
8. Acknowledgments	27
9. References	28

# 1 Introduction

At subduction zone, fluid transfer, tectonic processes and metamorphic reactions are tightly interconnected. The subduction of terrestrial material is accompanied by the change in metamorphic conditions which results in fluid production through compaction and mineral dehydration as sediments are buried and heated (Scambellur; Philippot, 2000). The fluids entering subduction zones on the incoming plate can be divided into two sources (a) the pore water in intergranular and fracture porosity in the sediments and (b) bound water within the hydrous minerals which is then liberated by dehydration reactions. The fluids along the plate interface of subduction zone influence small-scale mineral transformation and have also an impact on a large-scale geodynamic process, which in turn are necessary for geodynamic interpretations. Fluid inclusions are small tiny paleofluids that gets trapped in minerals which provide indispensable information about geological processes. The occurrence of fluid inclusions in the rocks and vein forming minerals provide an evidence of presence of fluids along the subduction slab. Further analysis of the fluid inclusions can place constraint on the composition and nature of fluids released at variable depths and their reaction transfers (Phillipot et al., 1993).

In the past 10-15 years, data from seismic imaging and drilling, instrumentation at the seabed and boreholes, geodetic and seismological observations have led to improved understanding of fluid flow and pore pressure in the subduction zones and their roles in volatile budgets and fault mechanism. Different models have been proposed to explain the pathway of fluids in subduction zone. (Peacock, 1990) propose that at shallow depth (< 40 km) in the subduction zone there is an expulsion and discharged of water into the mantle overlying the subducting slab. Also, (Philippot, 1993) contended that most of the water is released at shallower levels 0 –50 km and that only a small fraction of the initial water 10% is transferred into the subarc mantle via siliceous fluids or hydrous melts. Understanding the global geochemical cycles and element recycling during subduction is essential to understand the hydrodynamics of the deep parts of the subduction zones by determining the sources of fluids and the efficiency of fluid transfer from metamorphic sources. However, this aspect of the hydrodynamic models, which relates to transfers, is relatively poorly understood, mainly because the microscopic scale mechanisms that govern the transport of fluid in a solid matrix in plastic deformation are imperfectly described.

One possible way to analyze the exchange between a rock volume and the surrounding medium, in estimating to what extent a rock retains its original composition, is based on elemental or isotopic balances (Bebout et al., 2013). A complementary approach consists in analyzing the isotopic compositions of the calcite and quartz veins contained in the subducted sediments, considering that these veins were formed in equilibrium with the circulating fluid. However, the study of carbon and oxygen isotopes thus show that these fluids may have a contribution from deeper metamorphic fluids (Yamaguchi et al., 2012), although in other instances the isotopic compositions are buffered by reequilibration with the host rock (Raimbourg et al. Geosphere 2018). This extensive reequilibration with the host rock actually prevents these isotopes to clearly point to a clear origin for the “deep metamorphic fluids” and to discriminate the sources of fluids. Therefore, to understand the fluid transfer in the deep parts of the subduction zones, it is necessary to go beyond the traditional isotopes (C, O, H) in order to explore other signatures allowing the tracing of fluids involved in fluid/ rock exchanges characterizing the deep metamorphic aquifer.

Based on this idea, a preliminary work on quartz veins in the Alps oceanic domains (Flysch Helminthoid and Schistes Lustrés) is performed in order to understand how fluid circulation varies with metamorphic grade. (Raimbourg et al., 2018) studied the trace element concentrations of quartz by cathodoluminescence provided a strong contrast, in terms of hydrodynamics, between the deep part (in the plastic field) and the superficial part (in the brittle domain) of the subduction zone (Raimbourg et al., 2015). The deep part operates in a relatively closed system, and limits exchanges with the outside, and the superficial part is characterized by a cyclic alternation of two types of fluids, one local, the other exotic. However, the source of the exotic fluid is still unknown, and therefore in order to clarify its origin and the timing of its infiltration, a more precise work using isotopes of Ar is proposed. The approach used is via Ar-Ar in-situ UV laser ablation at the Ar-Ar laboratory, Institut des Sciences de la Terre d'Orléans. The application of the experimental techniques on the fluid inclusions helped to reveal the different compositional difference in a deformed and metamorphosed low-grade high-pressure terrain.

(M.A. Kendrick et al., 2007) studied the fluid inclusions in the different quartz veins at the giant Ernest Henry iron oxide–copper–gold deposit northwest Queensland. In this study, a combination of thermal and mechanical decrepitation methods enables distinction between four types of fluid inclusion. They reported that the fluid inclusions have compositions that define two end-members that are variably mixed in different samples. The first end-member has a  $^{40}\text{Ar}/^{36}\text{Ar}$  value of  $\sim 29,000$ ,  $^{40}\text{ArE}/\text{CL}$  value of  $\sim 3 \times 10^{-3}$  and mantle-like  $\text{Br}/\text{Cl} \sim 1-2 \times 10^{-3}$  and  $\text{I}/\text{Cl} \sim 11 \times 10^{-6}$ . The second end-member has a much lower  $^{40}\text{Ar}/^{36}\text{Ar}$  of  $< 2500$ , a  $^{40}\text{ArE}/\text{Cl}$  value of  $\sim 10^{-6}$ , and lower values of  $\text{Br}/\text{Cl} \sim 0.4 \times 10^{-3}$  and  $\text{I}/\text{Cl}$  of  $1-2 \times 10^{-6}$ . The data provide insight on the composition of crustal fluids and geochemical characteristics which are interpreted to provide insight on recycling at subduction zones and the composition of seawater. In 2006, (M.A. Kendrick et al., 2006) also had a Noble gas and Halogen constraints on mineralizing fluids present in quartz and dolomite veins to understand the metamorphic versus surficial origin at Mt Isa, Australia. They have investigated the origin of the hydrothermal fluids responsible for silica-dolomite alteration associated with Cu ore in the Mt Isa. They propose that the alternative origins of fluids between the metamorphic fluids and the surface-derived fluids could be distinguished by  $^{40}\text{Ar}/^{36}\text{Ar}$  and  $^{36}\text{Ar}$  concentration. They have reported that the metamorphic fluids have lower  $^{36}\text{Ar}$  concentrations, and  $^{40}\text{Ar}/^{36}\text{Ar}$  in the range 10,000-28,000 and high  $^{40}\text{ArE}/\text{Cl}$  values of  $3.8 \sim 10^{-4}$ . In contrast, the surface-derived fluids have elevated  $^{40}\text{Ar}/^{36}\text{Ar}$  values and high  $^{36}\text{Ar}$  concentrations.

In this study, the main focus of this work is to have the signature of isotopes from the fluids trapped in quartz veins during deformation (fluid inclusions), in two contrasted units of the oceanic domains of the Alps (Helminthoids Flysch and Schistes Lustrés). Determining the Ar isotopes from the fluid inclusions, is applied to give us more information about the origin and nature of the trapped fluids using the  $^{40}\text{Ar}/^{39}\text{Ar}$  in-situ technique. The in-situ technique provides the control on texturally-tied fluid inclusion populations or fluid inclusion generations coexisting side by side at the scale of the fluid inclusion distribution.

## 2 Geological Background

The tectonic evolution of the Western Alps is related to the closure of the Alpine Tethys, the north–south trending Valais and Liguro-Piemontese oceans from 100 Ma onward (Agard et al., 2002, Agard et al., 2009). The Western Alps resulted from successive subduction, accretion and

collision between the European and Apulian/African plates at rates less than 20mm/year from the Cretaceous to the Oligocene. Different geological objects corresponding to different stages of accretion can be recognized. The Western Alps are characterized by a very complex tectonic system. Stacks of continental and oceanic nappes formed during subduction and exhumation of the Jurassic Tethyan seafloor and associated European thinned margin below the Apulian plate (Agard et al., 2002, Angiboust et al., 2009). The general stratigraphy of the Alpine tectonic units consist of Mesozoic successions resting on continental basement rocks and on Carboniferous-Permian volcanic and sedimentary rocks, which are overlain by middle Eocene-Lower Oligocene Alpine Foreland Basin Successions. All these units are overthrust by Lower Cretaceous-lower-Paleocene Western Ligurian Flysch units (Piana et al., 2009).

There are many domains in the Western Alps with different types of rocks and sediments representing different ages. A zone of internal high-pressure metamorphic rocks to very low grade and non-metamorphic rocks occurs. The main paleogeographic domains are the Alpine Foreland Basin (For) succession, Western Ligurian Flysch (WestLF), Piemontese and pre-piemontese Domain (Pm+PPm), Briançonnais domain (IBr, EBr, ILBr) Provençal domain (Pro), Dauphinois domain (Dau) and the Argentera Crystalline Massif (ARG). The different metamorphic zones are Demonte-Aisone zone (DAZ), Limone-Viozène zone (LIVZ), Refrey zone (REZ) and Gardetta zone (GAZ). However, in this study the units studied belong to the Piemontese and Pre-Piemontese Domain (Pm + PPm) consisting of metasediments (Schistes lustrés) and the Western Ligurian Flysch units belonging to the oceanic domain (Fig. 1). The western part of the Ligurian Alps, the Argentera Massif, includes metasedimentary rocks and mylonites derived from high-grade metamorphic rocks (Bogdanoff 1986). The Dauphinois domain together with Provençal domain represents the more internal part of the European proximal (Mohn et al., 2010) developed above the Argentera Massif. The Briançonnais domain is located between the Mesozoic Ligurian-Piemonte basin and the Dauphinois and Provençal domains. The Ligurian-Piemonte (study area) lies north of the Briançonnais domain. The Western Ligurian Flysch lies north of Argentera Massif. The Briançonnais is stacked between the Piemontese and pre-piemontese Domain (Pm+PPm) and Western Ligurian Flysch.

The Piemontese domain can be divided into two main tectono-metamorphic domains. To the west external zone of Liguro-Piemontese corresponds to a fossil accretionary wedge, the Schistes Lustrés domain, with lenses of mafics and ultramafics embedded in blueschist-facies, late Mesozoic metasedimentary rocks (Agard et al., 2001, Agard et al., 2002). To the east of this domain, the Monviso ophiolite forms the structural base of the Liguro-Piemontese domain which is separated from the adjacent Schistes Lustrés domain by an extensional shear zone (Ballevre et al., 1990). The Schistes Lustrés complex is composed of Upper Mesozoic pelagic metasedimentary rocks (Agard et al., 2001) with P-T conditions from 1.2-1.3 GPa – 350°C to 1.8-2.0 GPa- 500°C. The Schistes lustrés complex is a large portion of the Ligurian oceanic basement, which is subducted down to blueschist and eclogite facies conditions during the Alpine orogenesis (Agard et al., 2000). In the studied area the Schistes Lustrés are affected by an increase in metamorphic grade from west to east (Chopin and Schreyer, 1983). The common mineral assemblage contains quartz and relics of HP minerals carpholite or lawsonite formed at peak metamorphic conditions of 350-380°C and 15 kbars. The SL unit represent a westward-dipping schistosity

and is also marked by an east-west stretching lineation (Caron, 1977). The first deformation event D1 took place under HP blueschist facies condition which resulted in isoclinal folds and associated sequence repetition (Caron., 1977). Two other distinct deformation event D2 and D3 took place during exhumation were regarded as compressive events but were recently interpreted as extensional movements (Agard et al., 2000). The evidences at small scale are represented by syn-metamorphic veins. The SL metapelites contain HP index mineral carpholite, occurring together with quartz in the veins formed at metamorphic conditions of 350-380°C and 15kbars.

The Western Ligurian Helminthoides Flysch units also known as *Embrunais-Ubaye nappes* to the north of Argentera Massif (Kerckhove, 1969) are stacks of tectonic units of Lower Cretaceous- lower Paleocen deep water sediments detached from the original basement. Flysch Helminthoides (FH) unit constituted of ~1000m thick series of calcareous turbidites overlying a level of dark pelites containing sandstone beds (Kerckhove et al., 2005). The FH is associated to the Liguro- Piemontese oceanic domain like the Schistes lustrés unit (Kerckhove, 1963). The deformation in the nappe comprise of two phase of folding occurring at low-grade conditions of greenschist- facies conditions. The early stage deformation is recorded by isoclinal folding orientated NE-SW direction (Merle and Brun.,1981). The deformation develops a schistosity as axial planes of folds, and these folds are cut by numerous quartz veins perpendicular to bedding. The quartz vein represent early-stage deformation as they are refolded by isoclinal folds.

In contrast to the Schistes Lustrés, the absence of high-pressure minerals suggest that burial was much more limited. Maximum temperature conditions are also lower than in the SL, of the order or below 300°C (Raimbourg et al., Geosphere 2018), roughly similar to the conditions of the Massif Cristallins Externes, the surrounding continental terranes (Bellanger et al., J. Geodynamics 2015). The SL and the FH correspond therefore to similar paleogeographic domains, i.e. turbidites overlying an oceanic basement, but they were buried to very different depths. While the SL went down to blueschist-facies-conditions, the FH was buried down to much lower (yet not clearly estimated) depths. These two units enable therefore to assess the evolution of the fluid composition along the subduction interface across a large depth range.

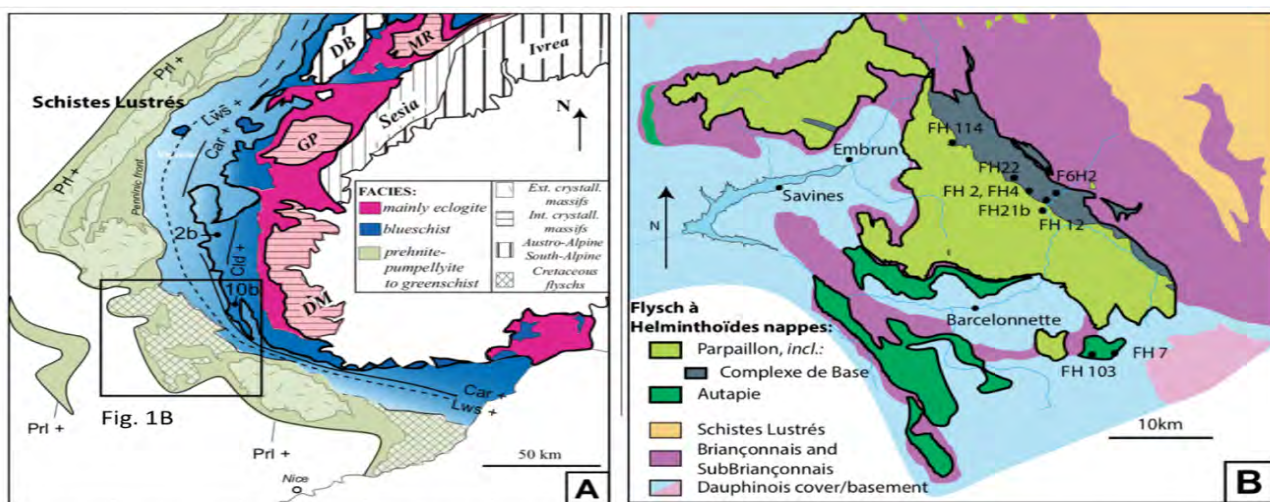


Fig.1: Geological map of the Alps showing the position of the two units studied in this study Modified from Agard and Lemoine (2003). (a)Both units Schistes lustré and Flysch Helminthoids (b) Close up view of Flysch Helminthoids.

### 3 Analytical Technique

#### 3.1 Sample Selection

The quartz viens that were selected from both units have a contrast in metamorphic temperature, one high-T (~350°C) unit and the other of low-T (~250°C) defined from Raman Spectrum of organic

matter (Raimbourg et.al., 2018). The two samples were processed to thin sections for optical microscopy for detailed petrographic study.

### 3.2 Sample Preparation

The quartz minerals from the different units was selected and prepared for the irradiation process at the laboratory at ISTO in the form of thin-disk-shaped slices of thickness of 200  $\mu\text{m}$  and radius of 10 mm. The thin quartz mineral was prepared in such a way as to allow optical examination with a petrographic microscope, followed by isotopic analysis for the experimental approach by In-situ laser ablation. The quartz mineral was encapsulated in small aluminium disk of 10 mm size radius along with the irradiation standards FC sanidine. The prepared sample were then sent for irradiation at the TRIGA Nuclear reactor at Oregon States University, Corvallis, Oregon. The irradiation process was 36 hours long.

During the irradiation process,  $^{39}\text{Ar}$  in each sample is created by bombarding it with fast neutrons in a nuclear reactor. The  $^{39}\text{Ar}$  serves as a proxy for the  $^{40}\text{K}$  parent isotope; this works because the  $^{39}\text{K}$ : $^{40}\text{K}$  ratio is constant in Earth. The  $^{39}\text{Ar}$  atoms are created when these neutrons are absorbed by  $^{39}\text{K}$  atoms and the nuclear reaction:  $^{39}\text{K}(n,p)^{39}\text{Ar}$  occurs. To estimate the efficiency of this reaction, the samples are irradiated along with standard minerals whose age is known independently (FC sanidine, 28.02 Ma). Once the samples are returned from the reactor, we can measure the isotopic composition of the argon, to obtain the  $^{40}\text{Ar}/^{39}\text{Ar}$  ratio and solve the age equation to obtain an age.

### 3.3 Experimental Noble gas extraction technique

The noble gas extraction from the sample can be done by different method such as the step crushing, in-vacuo crushing, stepped heating or laser ablation, and combinations of these techniques can be employed to provide information about the distribution of noble gases and halogens in the sample. In this study the method for noble gas extraction was by the in-situ 213 nm deep-UV laser ablation at technique only. The application of the experimental techniques helped to reveal the compositional difference in Ar isotopes from the different fluid inclusions belonging to different textural setting and units of deformed and metamorphosed low-grade high-pressure terrain.

The ablation was applied on quartz mineral to measure the argon isotopes from the fluid inclusions. In most cases, the laser spot size is much larger than individual fluid inclusions, hence ablation release the gas contained in a cluster of fluid inclusions. The size and depth of the ablation pits was varied in order to obtain sufficient signals for the different Ar isotopes. For this study, a spot size of about 100-150  $\mu\text{m}$  was used for the ablation process and ablation pits were excavated to an estimated depth of 200-300  $\mu\text{m}$ . Noble gas released from fluid inclusions are purified using Zr-Al getter pumps that remove the major volatiles (e.g.  $\text{H}_2\text{O}$ ,  $\text{CO}_2$ ). A typical purification protocol would be to expose the extracted sample gas to two hot (250°C) SAES getters for 6 min; before admission into the mass spectrometer (Helix SFT model, Thermo Fisher).

A total of 296 spot measurements were made on quartz minerals from 11 samples. Each measurement procedure was in the order (1) Measurement of blank (2) concentration measurement of sample. Mean blanks for  $^{40}\text{Ar}$ ,  $^{39}\text{Ar}$ ,  $^{38}\text{Ar}$ ,  $^{37}\text{Ar}$  and  $^{36}\text{Ar}$  were  $1.242 \times 10^{-4}$ ,  $1.686 \times 10^{-7}$ ,  $6.440 \times 10^{-8}$ ,  $1.022 \times 10^{-6}$ ,  $5.437 \times 10^{-7}$  respectively. The blank are mostly very small and negligible for laser ablation.

## 4 Petrographic Study of Samples

From microscope petrographic study, few samples chosen for in-situ laser ablation have been studied. The distribution of fluid inclusion and the association of fluid inclusions with solid inclusions in the host crystal is the main focus in order to have the best constraints on the types of fluid inclusions with

the different type of textural setting. The distribution of fluid inclusions with their textural setting in both the units is reported in (Table. 4.1). The fluid inclusion can have a very complex parageneses. Some fluid inclusions are considered to be primary fluid inclusions trapped during mineral growth (Roedder, 1984). Other fluid inclusions have a density that varies with crystal domains, such as growth rims: for example some quartz have a fluid-inclusion rich core surrounded by a fluid inclusion poor rim. In such a configuration, whatever the nature of the fluid inclusions in the core, they predate the rim overgrowth. Finally, some secondary fluid inclusion are trapped along annealed fractures and post-date the mineral growth (Roedder, 1984).

#### 4.1 Flysh Helminthoides Samples

*Vein structure:* The large quartz veins associated from the Flysh Helmenthoids unit formed within the sandstone beds, perpendicular to bedding stratification. The sandstone beds, with the veins they bear, are affected by syn-subduction isoclinal folding, which suggests that veining is an early stage process.

*Quartz structure:* At thin section scale, quartz grains are coarse to medium size grains (~ 200 µm) having high abundance of fluid inclusions. Some samples have recrystallized quartz grains.

*Nature of the fluid in fluid inclusions/individual fluid inclusion shape and size:* The size of the fluid inclusion is generally < 5µm. Most fluid inclusions occur as two phase (liquid + vapour) with vapour bubble of varying size which account of about 30- 40% of the total volume (Fig4.1a). In addition, smaller inclusion are observed, with only one phase and no vapour bubble. Some samples have irregular decrepitated fluid inclusions of sizes < 10 µm.

*Distribution of the fluid inclusions:* The distribution and the abundance of fluid inclusion in one single quartz grain is very complex. One possible distribution of the fluid inclusions in the sample is as cluster of tiny fluid inclusions whose abundance is correlated with the growth rims of the crystal. For example, in Fig. 4.1.B, the abundance of fluid inclusions decreases sharply from the core of the quartz grain to its rim. Some decrepitated fluid inclusions are also randomly distributed within the quartz grains (Fig 4.1 e) Fluid inclusions occur also as trails along the micro cracks and grain boundaries (i.e. secondary fluid inclusions (Fig4.1 c and 4.1 d)). The common trails observed are intragranular (fluid inclusions confined to a particular mineral grain) and intergranular (trail of fluid inclusions crossing the grain boundary). Some irregular, lengthy and sometimes stretched fluid inclusions are randomly distributed (Fig. 4.1f). The fluid inclusions in Flysch Helminthoides are comparatively smaller in size than the fluid inclusions present in the Schist lustre samples.

#### 4.2 Schistes lustres Samples

The Schistes lustres complex is a portion of the Ligurian oceanic basement. It was buried down to HP-LT metamorphic condition grade from blueschist facies conditions to eclogite conditions.

The samples studied come from the transect near Sestrieres, Italy (Agard et al., 2001) and some quartz veins contain carpholite, which constrain the peak P-T conditions around 350-380°C and -15Kbar (Agard et al., 2000).

*Vein structure and composition:* The quartz veins present in the SL occur as large size (up to a few dm) lenses embedded in the foliation. The veins are composed of association of quartz and lawsonite, or quartz and carpholite. Lawsonite is particularly abundant in most of the samples, where it forms elongated light honey-coloured fibrous crystal of a large size. In most cases it was retrogressed during exhumation to an assemblage of calcite + phengite (Fig4.2 a). Calcite is also abundant in most of these samples having perfect cleavage with very high relief and colourless in plane polarised light.

Most calcite is from as result of retrograde reactions (Fig. 4.2 f). Carpholite is present as elongated fibers intimately intergrown with quartz (Fig. 4.2 c). At the thin section scale, fresh carpholite needles very long and thin (~ 30 µm) are distributed in quartz matrix and are associated with fluid inclusions. Thus, the close association of solid inclusions of carpholite needles and primary fluid inclusions is an evidence of the formation of these fluid inclusions at peak conditions.

*Quartz structure:* At thin section scale, the quartz grains vary from coarse to medium size (> 200 µm). They are elongated parallel to the direction of the foliation (Fig. 4.2 c). Based on the microscopic observations two types of quartz have been identified. Some samples have large quartz mineral with lower abundances of fluid inclusions with many cracks (Fig. 4.2 d), and the second type is identified to be highly recrystallized quartz grains (Fig. 4.2 e) and are highly deformed and some grains have been preserved from recrystallization. Few samples have tiny cracks fluid inclusions alignment sub-grain boundary and located in domain of large quartz grains.

*Fluid inclusion distribution:* The distribution of fluid inclusions within a single grain is very complex. There are different categories of fluid inclusions observed in the quartz grains of these samples.

*Isolated fluid inclusions:* Most of the fluid inclusion occur as isolated inclusions in deformed quartz grains containing fresh carpholite needles (Fig. 4.3a). They are generally of all sizes and scattered in a random array, of rounded to irregular shape. They occur mostly in two phase (liquid+vapour) and the smaller size fluid inclusion are mostly aqueous (Fig. 4.3 b). In many instances, these isolated fluid inclusions are decrepitated: they appear as a cluster with many very small satellite fluid inclusions around central, much larger ones with tortuous shapes (Fig. 4.3 c). Decrepitation of fluid inclusion takes place when there is a buildup of a significant differential pressure, i.e. contrast between the pressure of the fluid pressure and the host mineral. Some fluid inclusions are homogeneously distributed within a single grain (Fig. 4.3 c) and some decrepitated fluid inclusions occur within clear zone in a single grain (Fig. 4.3 d). *Inclusions along grain boundaries:* These types of fluid inclusion occurs as cluster and are located along boundary of sub-grain domain of large quartz grains. They are of irregular to rounded shape and most of them occur as single-phase (liquid) (Fig. 4.3e). They have very small sizes < 5µm. *Fluid inclusions along cracks:* Some fluid inclusion occurs as trails along the grain boundaries. They are generally small-sized, and numerous in number and are lengthy and stretched fluid inclusions (Fig. 4.3 f). Most of them occur as single-phase inclusions and a few two-phase inclusions were also observed.

Table 4.1. Description of the distribution of fluid inclusions in the units

Sample Number	Large Grains	Strain within large Grains	Decrepitated FI	Large Cracks	FI alignment subgrain boundary	FI trails	Mineral inclusion
SL-15-11			+				
SL-14-4	+	+	+	+	+	+	+
SL-15-2	+		+	+		+	+
SL-15-3B		+	+		+		
SL-15-1	+		+		+	+	+
SL-15-14	+		+	+			+
SL-15-13	+		+	+			+
SL-15-16		+	+		+		
FH4	+		+			+	
FH13	+					+	
FH2	+		+			+	
FH114	+		+		+	+	

FI- Fluid inclusions, SL- Shistes Lustre Samples, FH- Flysh Helminthoids Samples

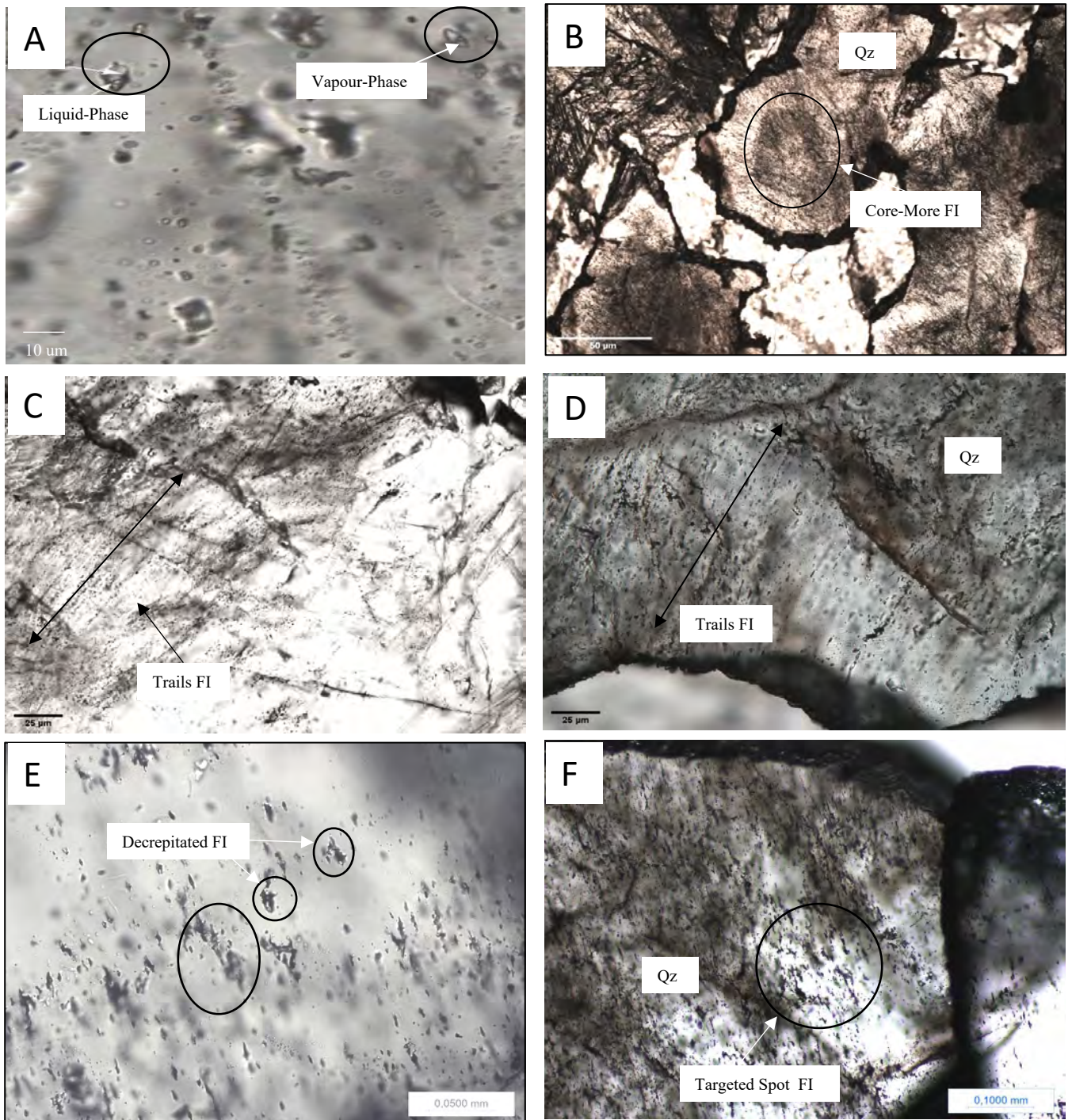


**Fig. 4.1: Petrographic study of the fluid inclusions in the Flysch Helminthoides samples** (a) The distribution of fluid inclusions in quartz grains that occur mostly as two phases (liquid + vapour) with bubble size of varying size which account for about 30-40% of the total volume. (b) Course quartz grains at 5X magnification showing the distribution of fluid inclusions within a single grain. The abundance of fluid inclusions occur in a random manner and is more concentrated at the core of the grain compared to the rim of the quartz mineral. (c) and (d) This is another type of fluid inclusion that occur as trail interpreted as secondary fluid inclusions that occur along the micro cracks and grain boundaries. The terminology observed is intragranular (fluid inclusions confined to a particular mineral grain) and also intergranular (trail of fluid inclusions crossing the grain boundary). (e) Decrepitated fluid inclusions randomly distributed within the quartz grains. (f) High abundance of tiny fluid inclusions within a single quartz grain.

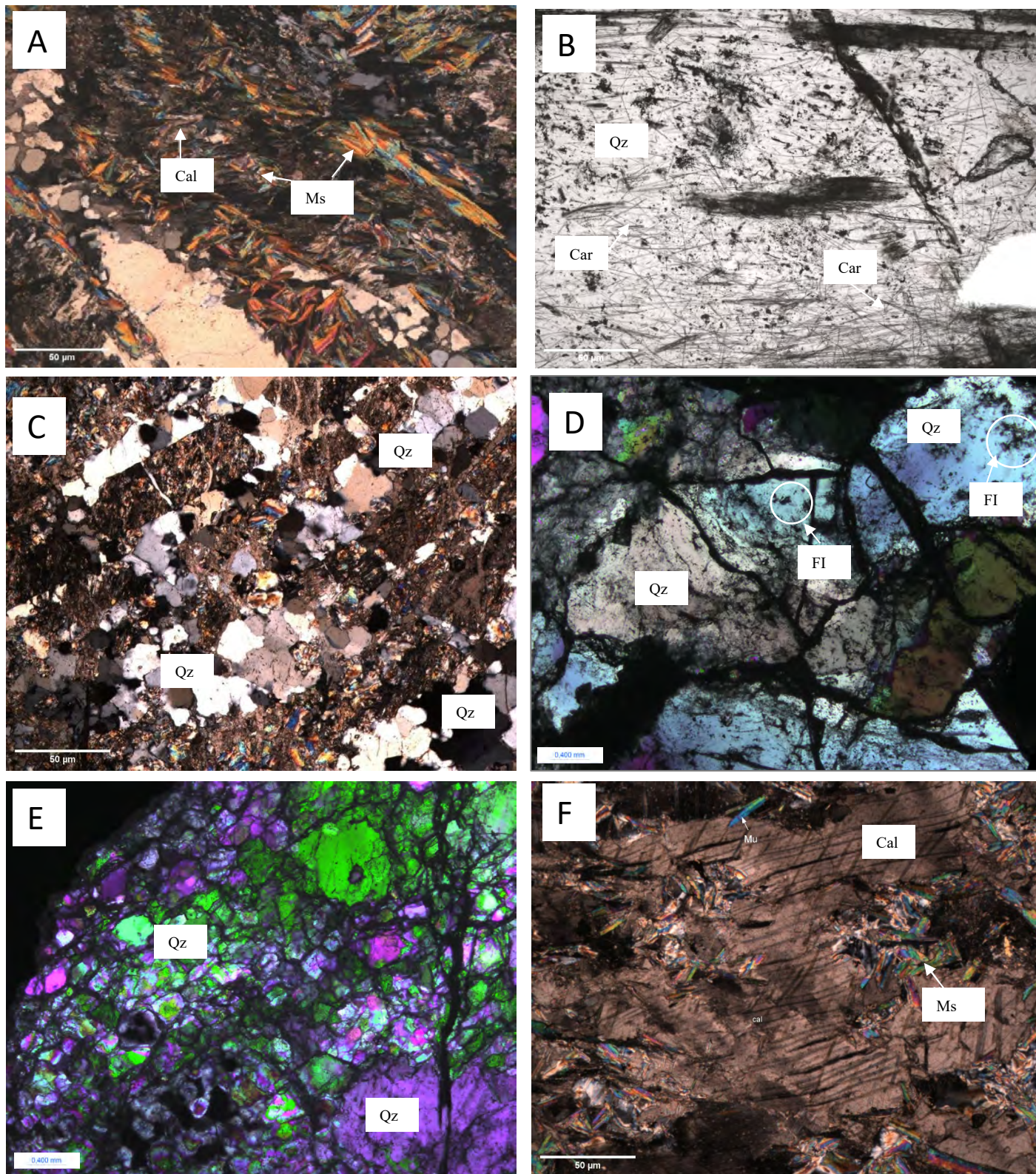


**Fig. 4.2: Petrographic study of the different paragenesis in the schist lustrous samples** (a) Elongated lawsonite fibrous crystal appear to be very coarse and may have been retrograde from high pressure conditions to lower pressure conditions and was replaced by calcite and phengite. (b) Carpholite a high pressure mineral index associated with quartz grains formed at peak metamorphism. The carpholite needles found in quartz grains are associated with fluid inclusions. (c) Quartz grains vary in size from coarse grains to medium size grains. They run along the direction of the foliation. (e) Recrystallized quartz mineral (d) Large quartz grains (f) Coarse calcite grain showing perfect cleavage with phengite minerals.

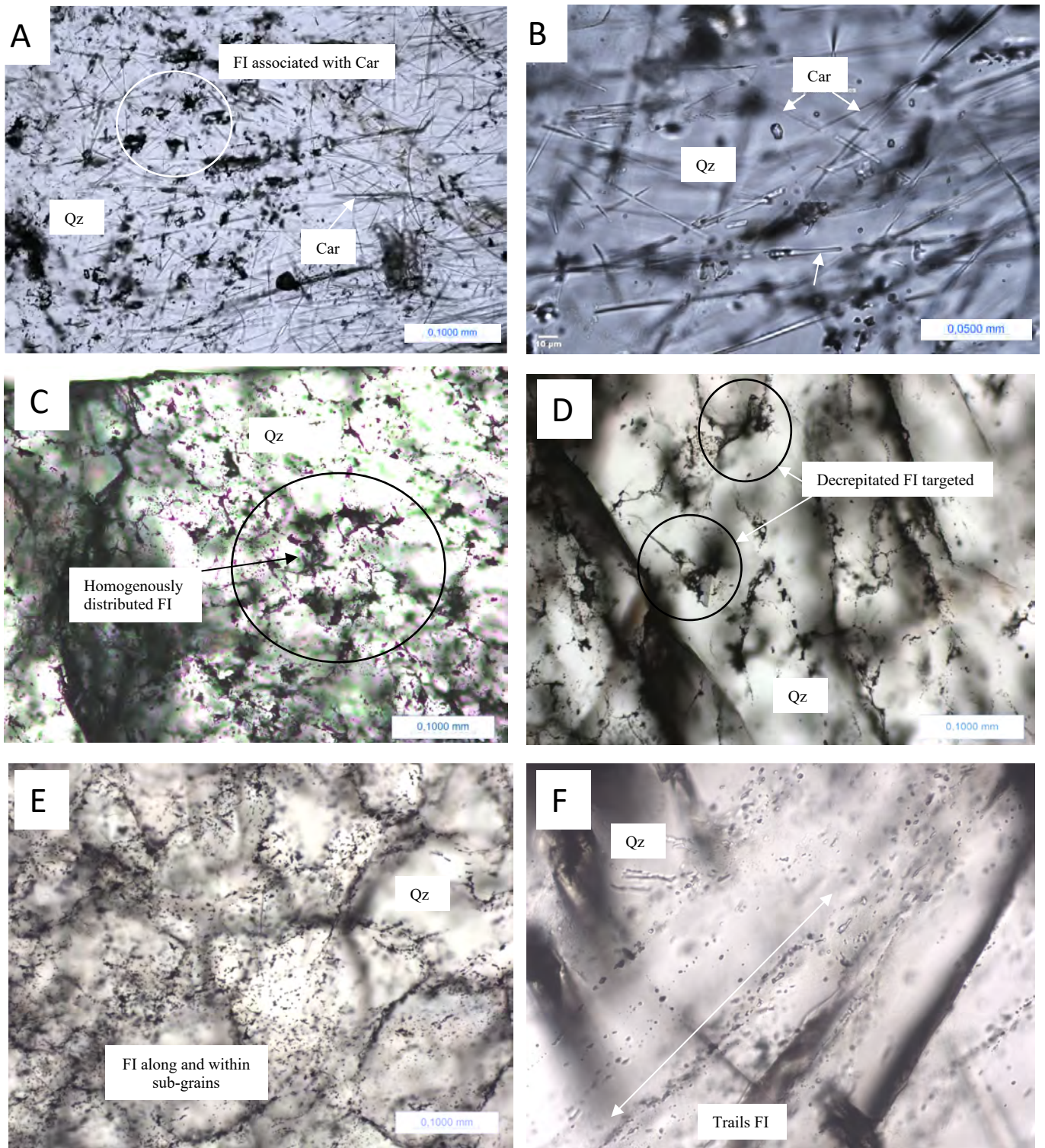


**Fig. 4.3: Petrographic study of the different types of fluid inclusions in the Schistes Lustrés samples** (a) Fluid inclusions occur as isolated inclusions in deformed quartz grains associated with carpholite needles (b) Two phase(liquid+vapour) inclusions with rounded to irregular shape and scattered in a random manner within the quartz grains.(c) High abundance of decrepitated fluid inclusions homogeneously distributed within a single grain.(d) Big decrepitated fluid inclusions in large quartz grains (e) The fluid inclusions occurring along the grain boundary of sub-grains of quartz.(f)Trails of fluid inclusions observed in quartz grains.

## 5. Results

The UV laser ablation was applied to the transparent quartz mineral from both the units. The compositional characteristics of the different fluid inclusions present in the quartz grains from the different units i.e, Flysh Helminthoides and the Schist Lustres are reported in Table. (5.1), (5.2) and (5.3). Based on the abundance of gas released it is likely that it was achieved on groups of fluid inclusions, rather than individual fluid inclusions in the majority of cases, depending on the texture and the areal density of the fluid inclusion relative to the spot size, i.e. the effective spacial resolution. Some cases the gas released was quantified on individual fluid inclusions present in the different units and textural settings.

### 5.1 Flysh Helminthoides Samples

Sample FH4, FH13, FH114 and FH2 were analyzed. All the samples have large quartz veins and are highly fractured with high abundance of fluid inclusion within a single grain. In the sample FH4, 24 points were chosen for analysis. There are three types of fluid inclusions characterize as decrepitated fluid inclusion, tiny rounded fluid inclusions and some occurring as trails of fluid inclusions. The gas released from the irregular fluid inclusions and decrepitated fluid inclusions show higher  $^{39}\text{Ar}_K$  compared to the fluid inclusions occurring as trails with lower  $^{39}\text{Ar}_K$  (Fig. 5.1a). The  $^{40}\text{Ar}_{tot}$  varies from different point analysis in the sample that ranges from  $1 \times 10^{-4}$  to  $7 \times 10^{-4}$  (Table. 5.1).

In the sample FH13, 25 points were chosen for the laser ablation. The tiny fluid inclusions occurring randomly within a single grain were the main target for analysis. There is a huge compositional difference among the points that are being analyzed. The single-phase fluid inclusion shows a high  $^{39}\text{Ar}_K$  abundances compared to the irregular two-phase fluid inclusions. The fluid inclusions occurring together show high  $^{40}\text{Ar}_{tot}$  in the order of  $3 \times 10^{-4}$  to  $4 \times 10^{-4}$  (Table. 5.1). The  $^{40}\text{Ar}_{tot}$  ranges from  $5 \times 10^{-5}$  to  $4.5 \times 10^{-4}$ ,  $^{36}\text{Ar}$  from 0 to  $1.4 \times 10^{-6}$  (Fig. 5.1 c and Fig. 5.1 e). In the sample FH114, 24 points were analyzed. The sample have large quartz veins with high abundance of fluid inclusions within a single grain and some quartz grains are recrystallized. The two types of inclusions occur as tiny two-phase fluid inclusions and irregularly shaped decrepitated fluid inclusions. Some irregular fluid inclusions occur along the sub-grain boundaries and also some occurring together with the tiny two-phase fluid inclusions. The gas released from the fluid inclusions present in this sample have higher isotopic values compared to the other FH samples. The irregularly shaped decrepitated fluid inclusions show lower abundance of  $^{40}\text{Ar}_{tot}$  and  $^{36}\text{Ar}$  compared to the two-phase fluid inclusions. The  $^{40}\text{Ar}_{tot}$  in this sample ranges from  $1 \times 10^{-3}$  to  $4.5 \times 10^{-3}$ ,  $^{36}\text{Ar}$  from 0 to  $1.8 \times 10^{-5}$  (Fig. 5.1 d and Fig 5.1 f).

In sample FH2, 25 points were analyzed. The quartz grains in this sample are large with high abundance of fluid inclusions and a few quartz grains are recrystallized. The fluid inclusions present in this sample can be characterized as two types the tiny two-phase fluid inclusion and the irregular shaped decrepitated fluid inclusions. The gas released from the fluid inclusions in this sample also have high isotopic values similar to sample FH114. The first few points were analyzed on decrepitated fluid inclusions show a higher  $^{39}\text{Ar}_K$  compared to the tiny two-phase fluid inclusions (Fig. 5.1 b). In this sample, it is also observed that the irregular shaped decrepitated fluid inclusions have higher  $^{40}\text{Ar}$  and  $^{36}\text{Ar}$  compared to the two-phase fluid inclusions. The  $^{40}\text{Ar}_{tot}$  ranges from  $1 \times 10^{-4}$  to  $1.7 \times 10^{-3}$ ,  $^{36}\text{Ar}$  from 0 to  $5.5 \times 10^{-6}$ . The fluid inclusions in the sample FH4 and FH13 have lower isotopes traces compared to the fluid inclusions in the sample FH114 and FH2. The ratio  $^{40}\text{Ar}_{tot}/^{38}\text{Ar}_{un}$  vs  $^{40}\text{Ar}_{tot}/^{36}\text{Ar}_{atm}$  was plotted and this plot shows a variation of the Ar isotopes ratio for the different points and types of fluid inclusions in different positions.

Table 5.1. Analysis for Flysch Helminthoides Samples

Sample Analysis	<sup>35</sup> Cl	<sup>39</sup> ArK	<sup>37</sup> ArCa	<sup>38</sup> ArCl	<sup>36</sup> Ar <sub>atm</sub>	<sup>40</sup> Ar <sub>tot</sub>	<sup>40</sup> Ar*	<sup>40</sup> Ar*/ <sup>39</sup> ArK
<b>FH4</b>								
Trails	3,615E-07	1,387E-07	3,156E-06	5,338E-08	5,927E-07	3,550E-04	1,799E-04	1,297E+03
	4,251E-07	-1,538E-08	1,173E-06	-1,014E-07	1,493E-06	5,613E-04	1,201E-04	-7,810E+03
	2,700E-07	2,372E-08	2,741E-06	-7,176E-08	9,111E-07	3,760E-04	1,068E-04	4,500E+03
Decrepitated	-1,244E-07	8,847E-08	1,080E-06	-2,794E-08	2,872E-07	1,109E-04	2,604E-05	2,943E+02
	-1,557E-07	8,229E-08	-1,342E-06	-3,271E-08	1,710E-07	1,202E-04	6,967E-05	8,466E+02
	6,832E-08	1,888E-08	9,398E-07	-1,148E-08	3,465E-07	2,428E-04	1,404E-04	7,438E+03
Tiny rounded	-1,409E-07	1,087E-07	5,491E-07	2,259E-08	3,674E-07	1,749E-04	6,633E-05	6,102E+02
	3,617E-07	-9,380E-09	9,398E-09	-4,028E-09	8,861E-07	4,794E-04	2,176E-04	-2,320E+04
	1,100E-08	1,395E-08	1,747E-06	-8,100E-08	1,681E-06	6,886E-04	1,918E-04	1,374E+04
<b>FH13</b>								
Single phase FI	2,902E-07	1,774E-07	7,905E-08	-4,273E-08	6,674E-07	2,132E-04	1,595E-05	8,988E+01
	1,692E-07	3,613E-07	-5,301E-07	-2,873E-08	6,068E-07	2,149E-04	3,560E-05	9,853E+01
	1,821E-07	1,566E-07	-5,620E-07	-3,372E-08	9,102E-08	7,116E-05	4,426E-05	2,826E+02
Bi-phase FI	-3,623E-07	7,358E-08	-2,465E-06	7,150E-09	3,877E-07	1,605E-04	4,599E-05	6,251E+02
	-2,234E-07	1,850E-08	8,365E-07	-4,630E-08	9,052E-07	2,912E-04	2,375E-05	1,284E+03
	-3,232E-07	1,863E-08	-3,478E-07	-4,609E-08	6,407E-07	2,454E-04	5,611E-05	3,012E+03
<b>FH14</b>								
Decrepitated FI	3,377E-07	9,146E-08	-3,571E-07	-8,502E-08	4,397E-06	1,348E-03	4,812E-05	5,261E+02
	3,922E-08	8,992E-08	-1,411E-06	-1,072E-07	1,592E-05	4,690E-03	-1,611E-05	-1,792E+02
	-1,216E-07	2,354E-07	-4,217E-07	-7,653E-08	4,981E-06	1,543E-03	7,134E-05	3,031E+02
Bi-phase FI	8,968E-08	1,494E-07	8,746E-07	1,306E-08	6,447E-06	1,919E-03	1,422E-05	9,514E+01
	5,283E-07	2,630E-07	-1,730E-07	-1,459E-07	7,576E-06	2,350E-03	1,110E-04	4,220E+02
	-7,384E-08	2,003E-07	4,033E-06	-7,029E-09	3,483E-06	1,126E-03	9,670E-05	4,828E+02
<b>FH2</b>								
Decrepitated FI	1,573E-08	2,177E-08	6,109E-06	3,071E-08	7,646E-07	3,560E-04	1,301E-04	5,977E+03
	1,690E-07	1,637E-07	1,975E-06	4,567E-08	2,784E-06	8,544E-04	3,177E-05	1,941E+02
	-3,004E-07	1,352E-07	-1,909E-06	-2,291E-08	2,839E-06	9,291E-04	9,036E-05	6,684E+02
Bi-phase FI	8,590E-08	7,275E-08	8,811E-07	-1,788E-08	1,113E-06	4,602E-04	1,313E-04	1,805E+03
	-1,314E-07	9,972E-09	-1,987E-06	-8,671E-08	3,115E-06	1,031E-03	1,103E-04	1,106E+04
	1,667E-08	1,628E-08	-4,840E-07	-5,065E-09	2,109E-07	1,757E-04	1,134E-04	6,966E+03

**FI: Fluid inclusions**

**LOWER ISOTOPIC VALUES SAMPLES**

**HIGH ISOTOPIC VALUES SAMPLES**

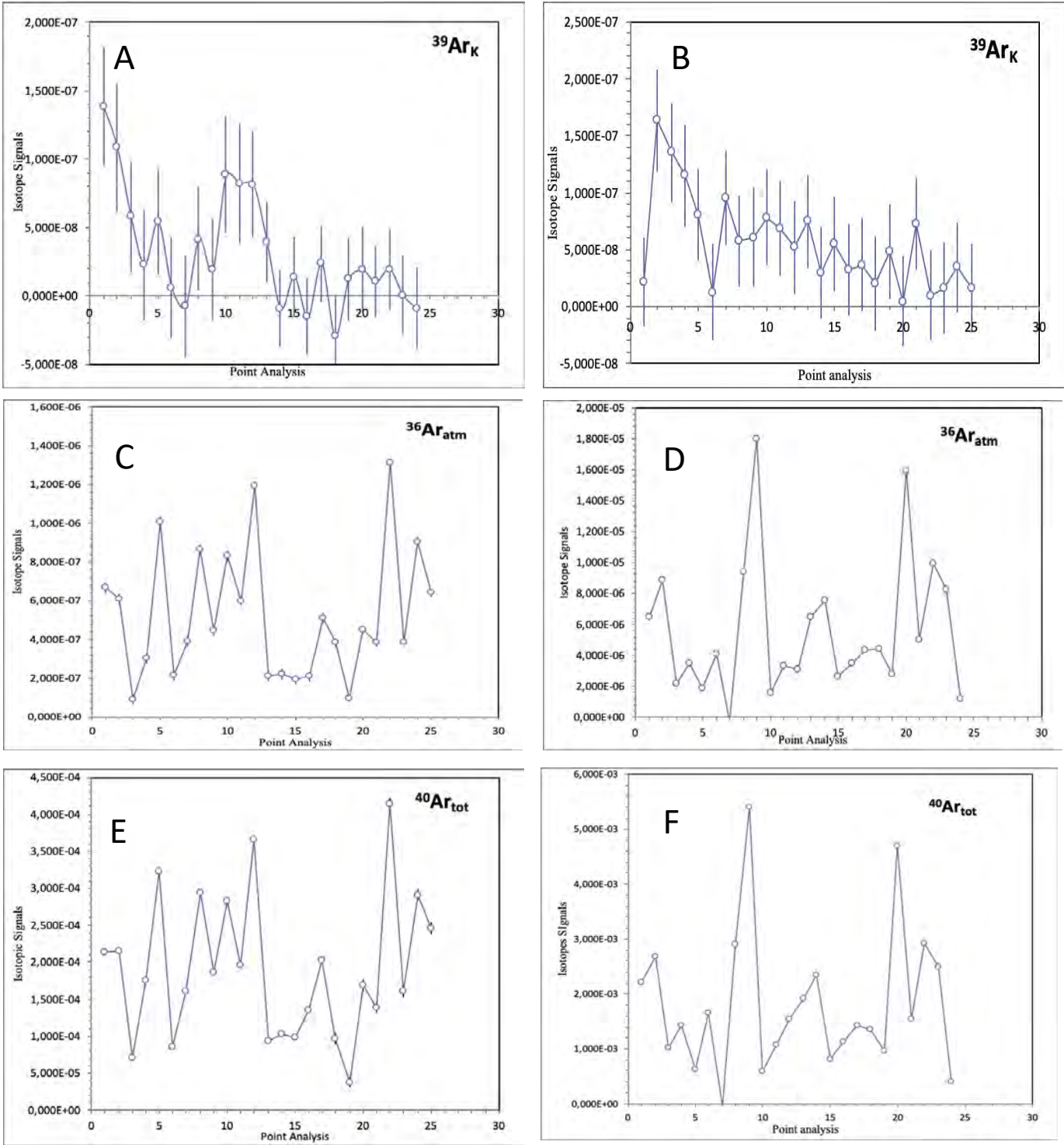


**Fig 5.1: Isotopic results from the occluded fluid inclusions in the Flysch à Helminthoides:**

(a) Irregular fluid inclusions and decrepitated fluid inclusions show higher  $^{39}\text{Ar}_K$  compared to the fluid inclusions occurring as trails with lower  $^{39}\text{Ar}_K$  in sample FH4 (b) The first few points were analyzed on decrepitated fluid inclusions and show a higher  $^{39}\text{Ar}_K$  compared to the tiny two-phase fluid inclusions in sample FH2.(c).  $^{36}\text{Ar}$  from  $0$  to  $1.4 \times 10^{-6}$  from the sample FH13.(d)  $^{36}\text{Ar}$  from  $0$  to  $1.8 \times 10^{-5}$  from the sample FH14.(e).  $^{40}\text{Ar}_{tot}$  ranges from  $5 \times 10^{-5}$  to  $4.5 \times 10^{-4}$  from the sample FH13 (f).  $^{40}\text{Ar}_{tot}$  ranges from  $1 \times 10^{-3}$  to  $4.5 \times 10^{-3}$  from the sample FH14 (y axis- abundance of isotope, x-axis – Point analysis)

## 5.2 Schistes lustrés

Sample SL-15-14, SL-15-3B, SL-15-1, SL-15-16, SL-15-2, SL-15-4 and SL-15-13 were chosen for Ar-Ar analysis. The samples are characterized based on the type of quartz grains. One type comprises of quartz mineral that are highly recrystallized quartz with comparatively less cracks and high abundance of fluid inclusion and another type is characterized by large quartz grains with lower abundance of fluid inclusions. In the sample SL-15-14, 55 points were chosen for analysis. The quartz grains include high abundances of fluid inclusions mainly characterize as decrepitated fluid inclusions, some of which are associated with solid mineral inclusions of carpholite, and two-phase fluid inclusions. The size of the decrepitated fluid inclusions in the range of  $5\mu\text{m}$  to  $10\mu\text{m}$  and in some cases the fluid inclusions are of bigger size. The gas released from the decrepitated fluid inclusions by in-situ laser ablation from this sample are comparatively higher compared to the other samples. There is a compositional variation from one point to another. The decrepitated fluid inclusion show a relatively high abundance of  $^{40}\text{Ar}_{\text{tot}}$  and  $^{40}\text{Ar}^*$  compared to the other types of fluid inclusions. (Fig. 5.2 e). The  $^{40}\text{Ar}_{\text{tot}}$  range from  $1\times 10^{-3}$  to  $9\times 10^{-3}$ ,  $^{36}\text{Ar}$  from  $1\times 10^{-5}$  to  $5\times 10^{-5}$  (Table. 5.2).

In the sample SL-15-3B, 25 points in the sample were chosen for analysis. This sample contain highly recrystallized quartz grains and some big quartz grains are preserved. The distribution of fluid inclusions is homogenous within a single grain. The fluid inclusions are characterized as two-phase fluid inclusions, decrepitated fluid inclusion with varying sizes, and some secondary fluid inclusions are distributed along the micro-cracks with irregular shapes. The gas released from the secondary fluid inclusions along the micro-cracks is characterized by high  $^{39}\text{Ar}_K$  in the range from  $4.5\times 10^{-7}$  to  $5.0\times 10^{-7}$ . The decrepitated fluid inclusions present together with the tiny two-phase fluid inclusions have  $^{39}\text{Ar}_K$  in the range from  $1\times 10^{-7}$  to  $2\times 10^{-7}$  which are comparatively lower than the fluid inclusions distributed along the micro-cracks (Fig 5.2 a). The fluid inclusion present at different textural positions have different abundance of gas with a variation in  $^{40}\text{Ar}_{\text{tot}}$  from one point to another (Table. 5.2) In the sample SL-15-1, 33 points were being analyzed. The quartz grains are large in size with high abundance of fluid inclusions of varying sizes approximately  $< 5\mu\text{m}$ . The sample contains big carpholite needles which are associated with the fluid inclusions. The types of fluid inclusions are characterized as decrepitated fluid inclusions with varying size, two-phase fluid inclusion, small elongate and irregular shaped fluid inclusions. The decrepitated fluid inclusions associated with the carpholites minerals have high  $^{40}\text{Ar}_{\text{tot}}$ . The gas released from a group of irregular shape fluid inclusions also have high abundance of  $^{40}\text{Ar}_{\text{tot}}$ . The small tiny fluid inclusions are characterized by high  $^{39}\text{Ar}_K$  compared to the other fluid inclusions in the range of  $1\times 10^{-7}$  to  $2\times 10^{-7}$ . The  $^{40}\text{Ar}_{\text{tot}}$  ranges from  $5\times 10^{-4}$  to  $4\times 10^{-3}$ ,  $^{36}\text{Ar}$  from  $2\times 10^{-6}$  to  $1.4\times 10^{-5}$ .

In the sample SL-15-16, 19 points were analyzed. Quartz grains in this sample are recrystallized to some extent and the larger quartz grains have undergone internal strain and some sub-grains are present within the larger quartz. There is a compositional variation from one point analyzed to another. Some smaller decrepitated fluid inclusions occurring together have higher  $^{40}\text{Ar}_{\text{tot}}$  compared to the bigger decrepitated fluid inclusions present individually. The  $^{39}\text{Ar}_K$  is in the range of  $1\times 10^{-8}$  to  $1.5\times 10^{-7}$ ,  $^{40}\text{Ar}_{\text{tot}}$  ranges from  $1\times 10^{-3}$  to  $5\times 10^{-3}$ ,  $^{36}\text{Ar}$  from  $2\times 10^{-6}$  to  $1.7\times 10^{-5}$  (Fig. 5.2 c). In the sample SL-15-2, 25 points are chosen for analysis with respect to the distribution of fluid inclusions. Quartz grains are large in size with lower abundance of fluid inclusions. In this sample, the decrepitated fluid inclusions are most common with varying sizes and some fluid inclusions occurring as trails and along the cracks. The bigger decrepitated fluid inclusions are present in very clear quartz grains. The smaller decrepitated fluid inclusions occurring together have higher  $^{39}\text{Ar}_K$  isotopic values compared to the bigger fluid inclusions (Fig. 5.2 b). The  $^{40}\text{Ar}_{\text{tot}}$  ranges from 0 to  $2.5\times 10^{-3}$ ,  $^{39}\text{Ar}_K$  from 0 to  $2.1\times 10^{-7}$ .

In the sample SL-15-4, 22 points were chosen for analysis. The quartz grains in this sample are large and have lower abundance of fluid inclusions within a single grain. The fluid inclusions can be

characterized as decrepitated fluid inclusion, rounded and irregular shape fluid inclusions which are randomly distributed and tiny fluid inclusion align along the grain boundaries. In this sample several bigger size decrepitated fluid inclusions were targeted individually. Similarly, there is a compositional difference of fluid inclusions occurring at different textural setting. The fluid inclusion that aligns along the grain boundary have lower  $^{39}\text{Ar}_K$  in the range of  $1 \times 10^{-8}$  to  $5 \times 10^{-8}$  compared to the tiny decrepitated fluid inclusions having signals of  $^{39}\text{Ar}_K$  in the range  $5 \times 10^{-8}$  to  $1.5 \times 10^{-9}$ . The  $^{40}\text{Ar}_{tot}$  range from  $1 \times 10^{-4}$  to  $2 \times 10^{-3}$ ,  $^{36}\text{Ar}$  range from  $1 \times 10^{-6}$  to  $8 \times 10^{-6}$  and  $^{40}\text{Ar}^*$  from  $1 \times 10^{-4}$  to  $2 \times 10^{-4}$ . In the sample SL-15-13, only 19 points were chosen for analysis. The quartz mineral in this sample are large and have lower abundance of fluid inclusion within a single grain. The size of the decrepitated fluid inclusion is approximately around 10-15  $\mu\text{m}$  and distributed randomly within the grains. The gas released from these fluid inclusions have lower abundance of  $^{39}\text{Ar}$  and  $^{40}\text{Ar}$  compared to the other samples. Similarly, there is a variation in the composition of isotopes from one fluid inclusion to the other. The larger size decrepitated fluid inclusion has more  $^{39}\text{Ar}_K$  and  $^{36}\text{Ar}$  compared to the smaller size fluid inclusions. The  $^{40}\text{Ar}_{tot}$  range from  $1 \times 10^{-4}$  to  $9 \times 10^{-4}$  (Fig. 5.2 f),  $^{36}\text{Ar}$  range from  $1 \times 10^{-7}$  to  $2.5 \times 10^{-6}$  (Fig 5.2 d) and  $^{40}\text{Ar}^*$  from  $1 \times 10^{-5}$  to  $1.5 \times 10^{-5}$ .

The gas released marked the isotopic variation among the fluid inclusions present at different textural setting. The fluid inclusions in the sample SL-14, 3B, 1 and 16 have higher isotopes content compared to the fluid inclusions in the sample SL-15-2, SL-15-4 and SL-15-13. Similarly, the fluid inclusions in the sample FH4 and FH13 have lower isotopes traces compared to the fluid inclusions in the sample FH114 and FH2. This can be explained based on the types of quartz mineral present in a sample. The fluid inclusions present in the highly recrystallized quartz grains have higher isotopic content compared to the fluid inclusions present in the bigger size quartz grains. The ratio  $^{40}\text{Ar}_{tot}/^{38}\text{Ar}_{un}$  vs  $^{40}\text{Ar}_{tot}/^{36}\text{Ar}_{atm}$  was plotted for all the samples and this plot shows a variation of the Ar isotopes ratio for the different points and types of fluid inclusions in different positions (Fig. 6.1). The gas released during the laser ablation could be a mixture of from different reservoirs, e.g., primary fluid inclusions and secondary fluid inclusions.

**Table 5.2. Analysis for Shistes lustre Samples**

Sample Analysis	<sup>35</sup> Cl	<sup>39</sup> Ar <sub>K</sub>	<sup>37</sup> Ar <sub>C<sub>2</sub></sub>	<sup>38</sup> Ar <sub>Cl</sub>	<sup>36</sup> Ar <sub>atm</sub>	<sup>40</sup> Ar <sub>int</sub>	<sup>40</sup> Ar <sup>w</sup>	<sup>40</sup> Ar <sup>w</sup> / <sup>39</sup> Ar <sub>K</sub>
<b>SL-15-14</b>	-1,658E-07	-1,140E-08	-5,588E-07	4,731E-09	1,054E-07	1,032E-04	7,205E-05	-6,319E+03
Decreepitated FI (Car)	3,723E-08	2,855E-07	1,092E-05	-3,910E-08	5,217E-06	1,703E-03	1,616E-04	5,659E+02
	5,009E-07	2,451E-08	1,555E-07	-8,549E-09	2,578E-07	3,417E-04	2,655E-04	1,084E+04
	1,855E-07	9,361E-08	6,483E-06	-2,609E-07	2,656E-05	7,597E-03	-2,517E-04	-2,689E+03
Big decreepitated FI	1,364E-07	6,568E-08	6,084E-07	-3,896E-08	3,609E-06	1,137E-03	7,031E-05	1,070E+03
	-1,566E-07	1,501E-07	-9,590E-07	2,175E-08	3,011E-05	8,852E-03	-4,535E-05	-3,022E+02
<b>SL-15-3B</b>	2,106E-07	1,298E-07	-5,701E-07	-4,397E-07	3,083E-05	8,873E-03	-2,387E-04	-1,839E+03
Decreepitated FI & bi-phase	6,169E-07	1,525E-07	-1,003E-06	-2,132E-07	2,618E-05	7,486E-03	-2,493E-04	-1,634E+03
	-5,931E-08	7,356E-08	-2,680E-07	-8,501E-08	1,440E-05	4,204E-03	-5,021E-05	-6,826E+02
	2,850E-07	4,610E-07	4,555E-06	-2,042E-07	2,379E-05	6,968E-03	-6,096E-05	-1,322E+02
FI in cracks	-3,129E-07	4,663E-07	2,493E-05	-6,974E-08	4,265E-06	1,496E-03	2,361E-04	5,063E+02
	-2,837E-07	3,704E-08	1,158E-06	-2,292E-08	1,176E-05	3,398E-03	-7,684E-05	-2,075E+03
	4,457E-07	9,512E-08	1,430E-06	-1,660E-07	7,695E-06	2,452E-03	1,785E-04	1,876E+03
Decreepitated FI	3,139E-07	9,354E-08	-1,912E-07	-2,703E-07	3,290E-05	9,515E-03	-2,079E-04	-2,223E+03
<b>SL-15-1</b>	2,855E-08	5,996E-08	2,817E-07	-1,289E-08	4,006E-06	1,256E-03	7,233E-05	1,206E+03
Decreepitated FI (Car)	-1,474E-07	9,318E-08	1,195E-06	-4,434E-08	3,320E-06	1,030E-03	4,868E-05	5,224E+02
	-2,228E-07	2,243E-08	1,740E-07	-1,278E-07	4,887E-06	1,472E-03	2,747E-05	1,225E+03
	3,022E-07	6,432E-08	4,110E-06	1,280E-07	1,429E-05	4,227E-03	4,006E-06	6,228E-01
	-6,946E-09	4,226E-09	1,742E-06	2,741E-09	4,851E-07	2,560E-04	1,126E-04	2,665E+04
Tiny FI	4,963E-07	8,225E-09	-2,822E-07	-4,372E-08	1,481E-06	4,653E-04	2,758E-05	3,353E+03
	3,947E-08	5,562E-08	-7,757E-07	-1,540E-08	4,184E-07	1,783E-04	5,463E-05	9,822E+02
<b>SL-15-16</b>								
Small decreepitated FI	-2,053E-07	1,117E-07	2,027E-06	-1,721E-07	1,742E-05	5,022E-03	-1,263E-04	-1,131E+03
	2,722E-07	1,362E-07	3,241E-06	-3,278E-08	4,127E-06	1,186E-03	-3,330E-05	-2,445E+02
	-1,175E-08	1,084E-07	1,689E-06	-1,247E-07	8,625E-06	2,497E-03	-5,170E-05	-4,771E+02
	9,227E-09	1,468E-07	-1,296E-06	-5,544E-08	2,635E-06	8,196E-04	4,113E-05	2,802E+02
Big decreepitated FI	1,139E-07	4,611E-08	1,573E-07	-1,102E-08	5,405E-07	1,985E-04	3,881E-05	8,417E+02
	-3,702E-08	5,748E-08	1,384E-07	-4,147E-09	3,900E-07	2,162E-04	1,010E-04	1,757E+03
	-1,479E-07	9,088E-08	-1,411E-07	-7,075E-08	1,663E-06	5,078E-04	1,624E-05	1,787E+02

FI: Fluid inclusions, Car: Carpholite mineral

**Table 5.3. Analysis for Shistes lustre Samples**

Sample Analysis	<sup>35</sup> Cl	<sup>39</sup> Ar <sub>K</sub>	<sup>37</sup> Ar <sub>C<sub>2</sub></sub>	<sup>38</sup> Ar <sub>Cl</sub>	<sup>36</sup> Ar <sub>atm</sub>	<sup>40</sup> Ar <sub>int</sub>	<sup>40</sup> Ar <sup>w</sup>	<sup>40</sup> Ar <sup>w</sup> / <sup>39</sup> Ar <sub>K</sub>
<b>SL-15-2</b>								
Bigger decreepitated FI	-1,922E-07	-8,506E-09	-1,528E-06	-5,820E-07	3,603E-06	1,845E-03	7,806E-04	-9,176E+04
	2,398E-07	1,046E-08	-1,035E-06	3,332E-09	8,469E-07	2,878E-04	3,749E-05	3,584E+03
	2,284E-07	1,652E-08	-1,075E-06	-1,036E-08	1,189E-07	1,173E-04	8,219E-05	4,975E+03
	1,854E-07	8,461E-09	6,349E-07	-6,961E-08	5,631E-07	2,081E-04	4,166E-05	4,924E+03
Smaller decreepitated FI	4,642E-07	4,468E-08	-7,504E-07	-3,042E-08	2,906E-06	1,056E-03	1,967E-04	4,403E+03
	7,514E-08	2,510E-08	3,856E-07	2,618E-09	3,012E-06	1,137E-03	2,469E-04	9,840E+03
	-1,780E-07	4,967E-08	3,787E-07	-1,781E-08	1,419E-06	5,535E-04	1,342E-04	2,701E+03
	4,281E-08	1,163E-07	9,857E-06	-1,345E-07	7,712E-06	2,351E-03	7,153E-05	6,151E+02
<b>SL-15-4</b>								
Rounded and Elogated FI	4,935E-07	3,020E-08	-1,257E-06	2,342E-08	-3,238E-08	-8,858E-06	7,112E-07	2,355E+01
	3,878E-07	-2,729E-08	1,395E-07	-1,430E-08	-3,196E-08	-1,293E-06	8,151E-06	-2,987E+02
	1,364E-07	-5,277E-08	4,965E-07	-2,257E-08	-1,858E-08	-2,737E-06	2,754E-06	-5,219E+01
Tiny FI along boundary	5,152E-09	3,159E-08	1,129E-06	-2,052E-08	4,436E-07	1,616E-04	3,047E-05	9,646E+02
	-2,048E-07	8,051E-08	-2,561E-07	-9,996E-08	3,759E-06	1,088E-03	-2,238E-05	-2,780E+02
	0,000E+00	1,630E-07	8,928E-07	-1,733E-08	9,057E-07	4,635E-04	1,959E-04	1,202E+03
	0,000E+00	5,680E-08	7,296E-07	-3,634E-08	1,804E-06	5,502E-04	1,719E-05	3,027E+02
	0,000E+00	9,052E-08	-9,589E-07	-1,169E-08	2,729E-06	9,111E-04	1,048E-04	1,158E+03
	0,000E+00	7,575E-08	-8,355E-07	-3,579E-09	3,222E-06	9,585E-04	6,266E-06	8,272E+01
Decreepitated FI	6,552E-07	1,215E-08	9,811E-07	-3,900E-09	2,602E-08	8,070E-06	3,802E-07	3,128E+01
	-1,658E-07	-1,165E-08	3,404E-07	-1,093E-08	5,344E-09	1,933E-06	3,537E-07	-3,037E+01
	0,000E+00	-5,154E-09	-1,139E-06	3,002E-08	5,848E-07	2,127E-04	3,990E-05	-7,742E+03
<b>SL-1513</b>								
Big decreepitated FI	3,878E-07	3,227E-09	3,904E-07	-5,757E-09	1,746E-07	6,828E-05	1,667E-05	5,165E+03
	1,364E-07	5,116E-08	1,594E-06	-2,745E-08	1,391E-06	4,272E-04	1,623E-05	3,172E+02
	3,654E-10	1,837E-07	1,456E-06	1,086E-08	3,575E-07	1,664E-04	6,073E-05	3,307E+02
	0,000E+00	4,615E-08	-8,153E-08	1,958E-08	1,039E-07	5,816E-05	2,744E-05	5,947E+02
Small decreepitated FI	-1,658E-07	9,438E-08	1,571E-06	-6,824E-09	3,811E-07	2,523E-04	1,397E-04	1,480E+03
	1,855E-07	4,237E-08	1,525E-06	-6,950E-09	1,449E-07	1,134E-04	7,062E-05	1,667E+03
	6,552E-07	5,731E-08	5,061E-07	-2,419E-09	3,496E-07	1,447E-04	4,136E-05	7,216E+02
	-9,643E-08	6,345E-08	-4,346E-07	-8,168E-09	1,435E-06	5,326E-04	1,087E-04	1,712E+03

FI: Fluid inclusions

## 6 Discussion

In this study, we have made a detailed petrographic microscopic study in order to understand the different types of fluid inclusions present at different textural setting within the different units. The present study was focused on the two units in the Western Alps, the Schistes Lustre and the Flysch Helminthoides. The fluid inclusions present in the Flysch Helminthoides are smaller in size compared to the fluid inclusions present in the Schistes Lustrés. The main objective is to have an isotopic analysis on the fluid inclusions from the two different units buried at different metamorphic conditions by using the in-situ laser ablation technique in order to test (1) whether they are compositionally different, (2) the length scale or textural control on potential isotopic heterogeneities or Ar reservoirs, and (3) the implications for the fluid circulation along the subduction zone.

*From the petrographic observations*, based on the quartz texture, the samples are divided into two types. The first (type-1) is characterized by big quartz grains with lower abundances of fluid inclusions, the second (type-2) quartz grains are recrystallized to some extent in the Schistes Lustre samples with higher abundance of fluid inclusions and finer quartz grains in the Flysch Helminthoides samples. (Fig. 6.1) show both (type-1) and (type-2) quartz grains from both the units.

*Correlation of petrographic observations and Ar/Ar isotope data*: The in situ Ar/Ar data reveal that the gas released from the fluid inclusions present in the highly recrystallized and the finer type-2 quartz have higher isotopic values ( $^{40}\text{Ar}_{\text{tot}}$  of  $4.706 \times 10^{-2}$ : and  $^{36}\text{Ar}_{\text{atm}}$   $2.077 \times 10^{-4}$ ) compared to the fluid inclusions present in the type-1 bigger size quartz grains having ( $^{40}\text{Ar}_{\text{tot}}$  of  $1.116 \times 10^{-2}$  and  $^{36}\text{Ar}_{\text{atm}}$   $3.171 \times 10^{-5}$ ) which is summarized in (Table. 6.1). The fluids trapped during recrystallization of the quartz mineral may have another component that is contributing to the isotopic variations. Noteworthy, small-scale isotopic variations also occur between the different point analysis within a single sample separated by few mm in distance. The differences in isotopic composition testify that temporal variations in fluid entrapment are associated with changes in fluid composition hence fluid source.

Observations with respect to the types of fluid inclusions and Ar/Ar data revealed that in the sample FH4 (Fig.6.2) there is no coherent isotopic trend, nor any apparent connection with a specific FI type or generation contributing to a particular isotopic component. However, most of the gas released are from groups of FI which includes both decrepitated fluid inclusions and tiny fluid inclusions. These groups of FI can be divided into two zones. The Zone-I, at the frontier part of the sample consist of decrepitated fluid inclusions, rounded FI and several tiny FI having lower  $^{40}\text{Ar}_{\text{tot}}$  values. The Zone-II, concentrated at the centre of the sample, consist of trails of fluid inclusions and tiny fluid inclusions having higher  $^{40}\text{Ar}_{\text{tot}}$  values. Similarly, the same observation has been made in Sample SL-15-2. There are a group of points analyzed from a particular zone which are separated by few millimeters in distance that contribute to a similar isotopic value (Fig. 6.2). Zone-I consist of few decrepitated FI marked higher  $^{40}\text{Ar}_{\text{tot}}$ . Zone-II, consist of bigger decrepitated fluid inclusions occurring together with small FI have lower  $^{40}\text{Ar}_{\text{tot}}$  values.

*Correlation of three-isotope plot and FI type*: A three-isotope correlation plot  $^{40}\text{Ar}_{\text{tot}}/^{38}\text{Ar}_{\text{run}}$  vs  $^{40}\text{Ar}_{\text{tot}}/^{36}\text{Ar}_{\text{atm}}$  from all the points analyzed from the Schistes Lustres samples (Fig. 6.3.a) and Flysch Helminthoides (Fig. 6.3b) have been plotted. *Firstly*, there is a difference between the isotopic abundance between the two units. The Schistes Lustres samples

have a higher isotopic abundance scattered in a large  $^{40}\text{Ar}_{\text{tot}}/^{38}\text{Ar}_{\text{run}}$  range from 0 to  $2.5\text{E}+04$ . The Flysch Helmenthoides sample plots at a lower  $^{40}\text{Ar}_{\text{tot}}/^{38}\text{Ar}_{\text{run}}$  range from 0 to  $5.0\text{E}+03$  compared to the Schistes Lustre. *Secondly*, the different samples (marked in different colours) from both the units show different isotopic abundance. Some samples have indistinguishable isotopic ratios plotting close to the atmospheric isotopic ratio (red point).

However, to be able to have a correlation of the three isotopes with respect to the FI population, a  $^{40}\text{Ar}_{\text{tot}}/^{38}\text{Ar}_{\text{run}}$  vs  $^{40}\text{Ar}_{\text{tot}}/^{36}\text{Ar}_{\text{atm}}$  plot of the FI population data for each sample have been plotted. There is a significant variation in Ar isotopes ratio from the different points that are analyzed and the types of fluid inclusions present in different textural positions.

Sample SL-15-14 (Fig. 6.4a), displays a trend in isotopic ratios moving along a positive slope away from the atmospheric ratio (red point). The theoretical trend plotted, provides an indication of addition of excess  $^{40}\text{Ar}$  concentration derived from the basement rocks during water-rock interaction. Most points plot along this trend. The isotopic ratio that are isolated from this trend point to a third (and maybe more) component also contributing to the variations in isotopic ratio, the source of which is currently unknown. There also exist a huge variation in the isotopic ratio in connection with the type of fluid inclusion analyzed. The decrepitated fluid inclusions associated with the solid inclusions of carpholite are characterized by distinctly higher isotopic ratio (marked in different colours) than the other types of fluid inclusions, notably the decrepitated fluid inclusions occurring together with the two-phase fluid inclusions showing an isotopic ratio in the range of  $6 \times 10^{+2}$  to  $8 \times 10^{+2}$ . Some decrepitated fluid inclusions show very similar isotopic values around range  $4 \times 10^{+2}$  to  $6 \times 10^{+2}$ . These ratios are nearer to the atmospheric isotopic ratio. Sample F114 (Fig. 6.4b) shows a more clustered plot nearer to the atmospheric ratio. The theoretical trend in isotopic ratios lies along a positive slope away from the atmospheric ratio providing the indication of addition of  $^{40}\text{Ar}$  from the basement rocks. The decrepitated fluid inclusions in this sample are characterized by higher isotopic ratio compared to the smaller size two-phase fluid inclusions. We infer that the decrepitated fluid inclusions have a non-atmospheric component contributing to the isotopic variations with the smaller size fluid inclusions contributing to a ratio closer to the atmospheric values.

## SCHISTES LUSTRE

## FLYSCH HELMINTHOIDES

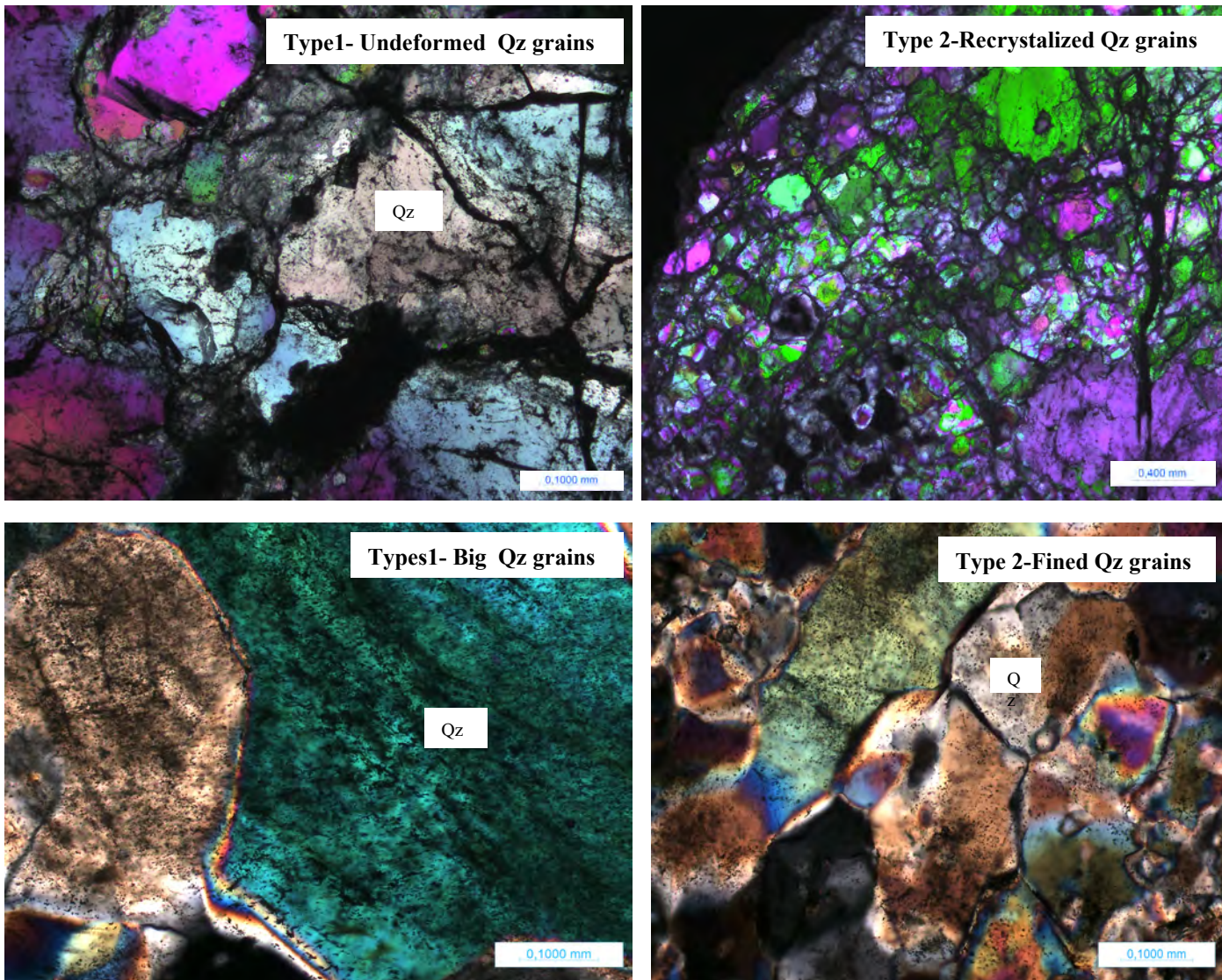
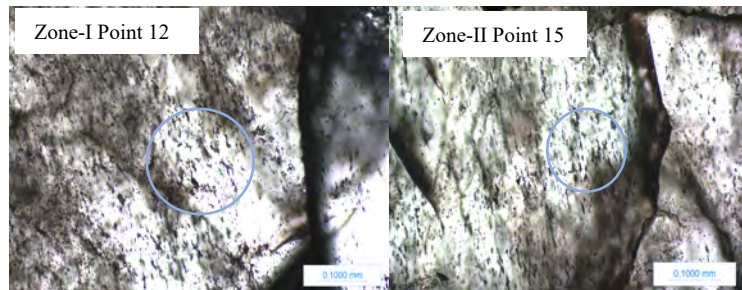
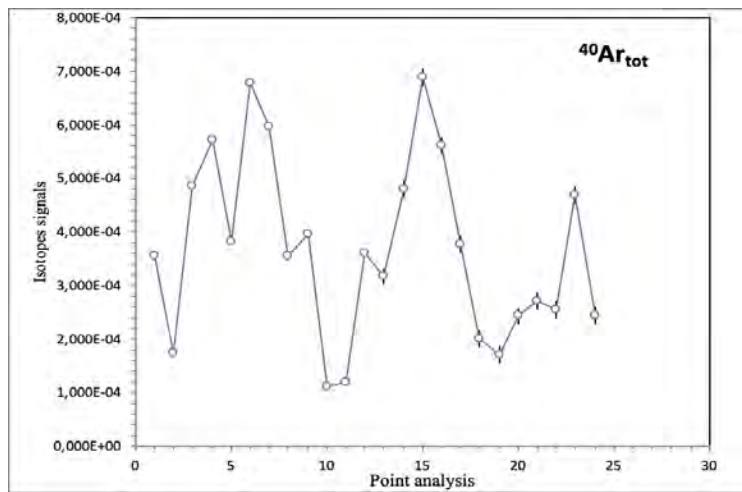
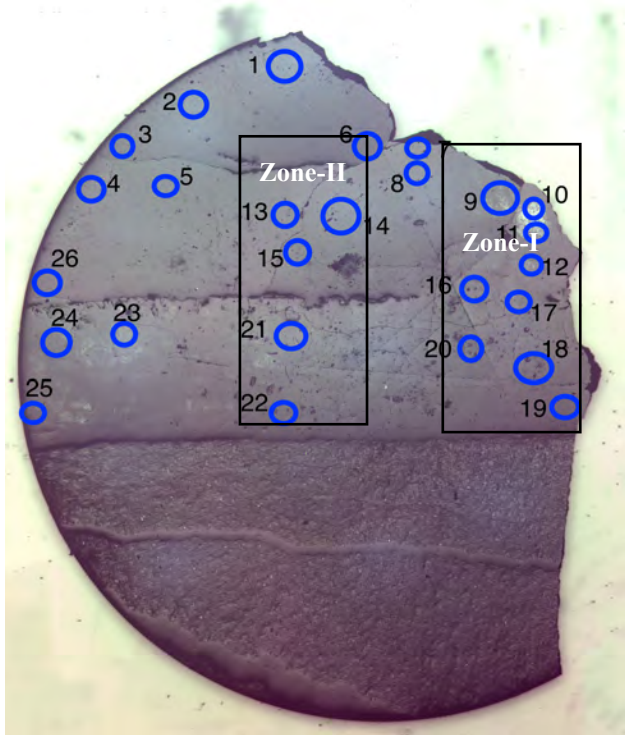


**Fig. 6.1: Petrographic micorscopic pictures of the different Units Schistes Lustre and Flysh Helminthoides with both types-1 quartz grains and type-2 quartz grains.**

## FLYSCH HELMINTHOIDES- FH4



## SCHISTES LUSTRE- SL-15-2

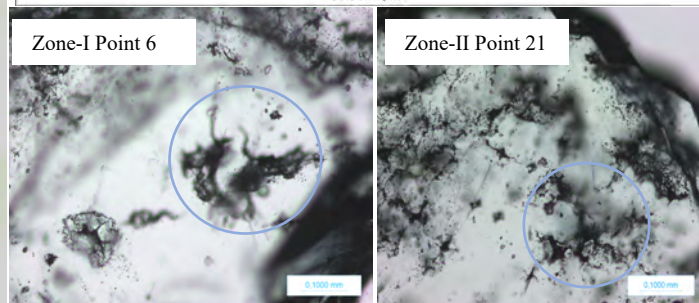
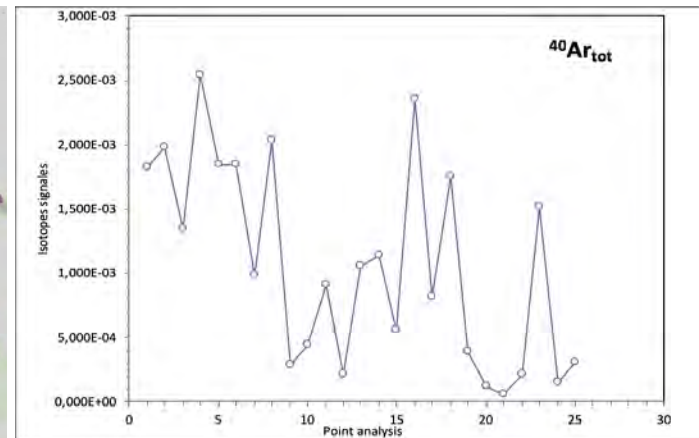
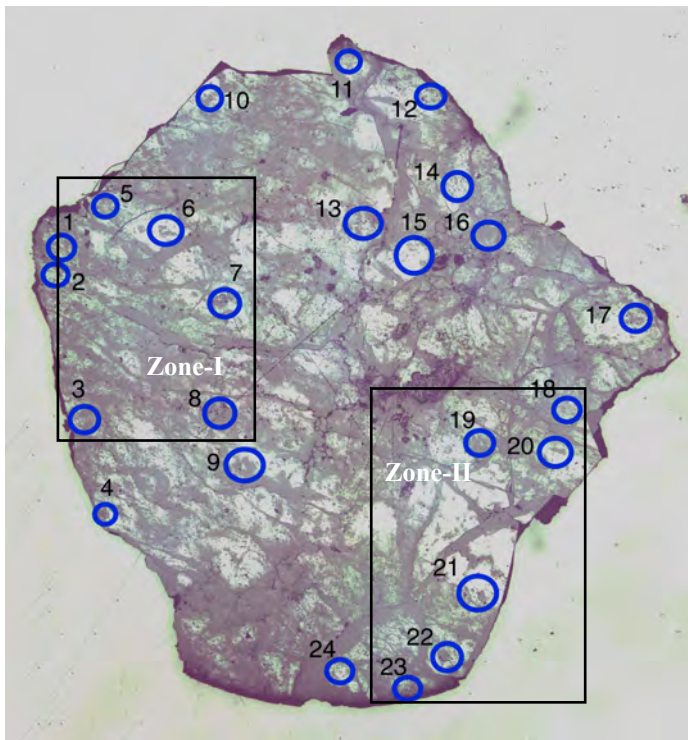
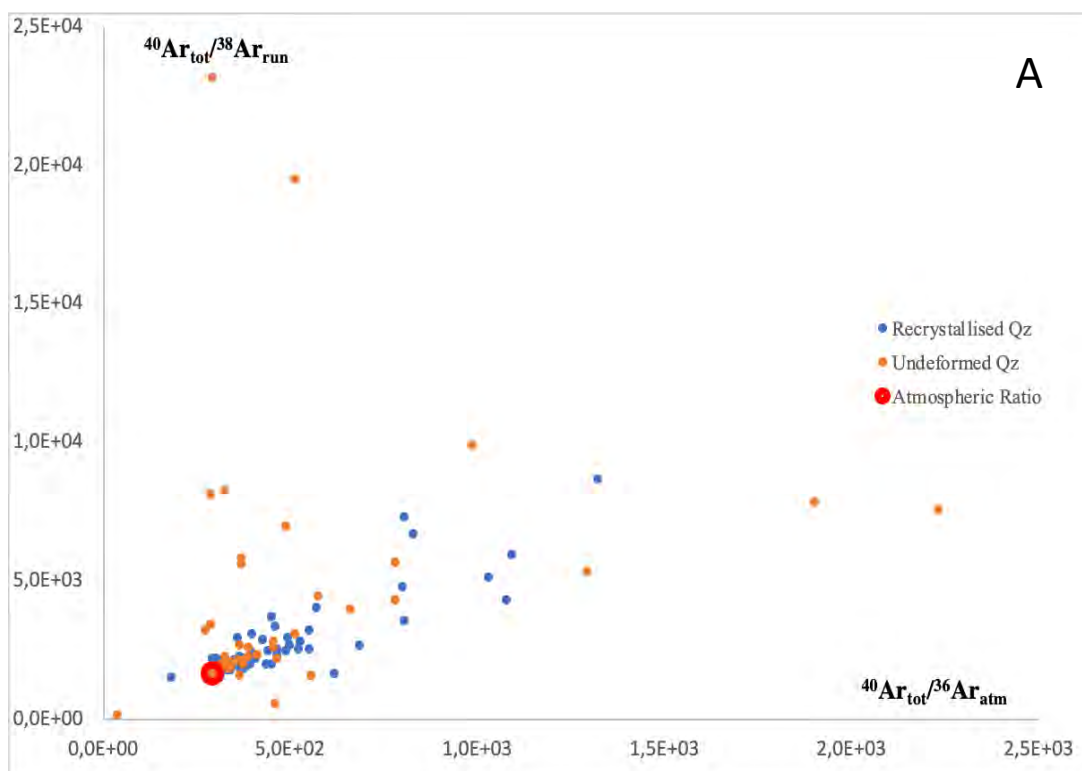


**Fig 6.2: Sample picture with different point analysis and micorscopic pictures of the different types of FI's representing the zone having similar isotopic variation. The  $^{40}\text{Ar}_{\text{tot}}$  plot showing variation in isoptic values from one point analysis to another.**

## SCHISTES LUSTRE



## FLYSCH HELMINTHOIDES

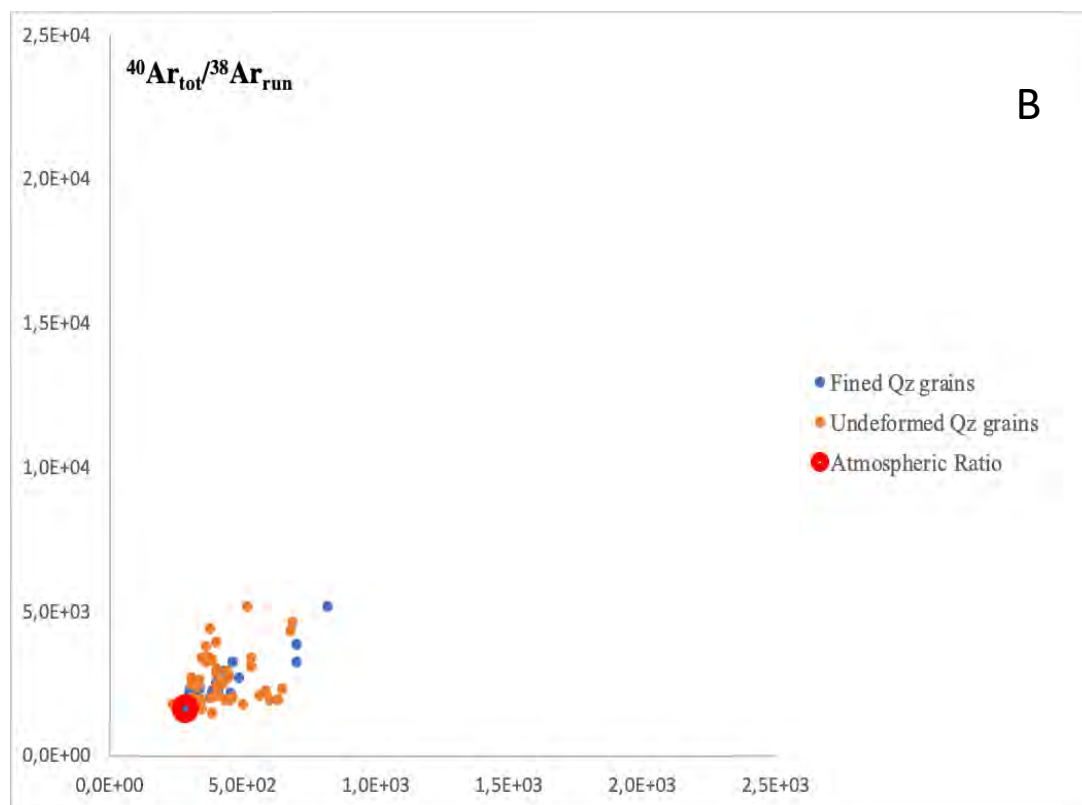
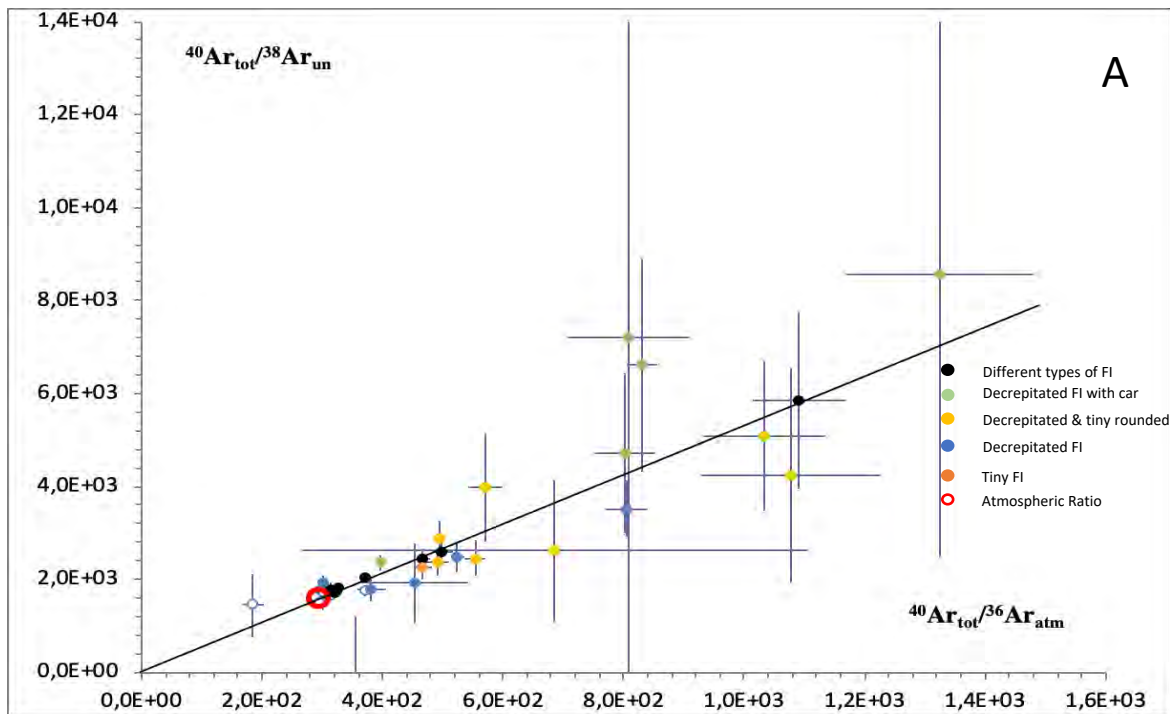


**Fig. 6.3  $^{40}\text{Ar}_{\text{tot}}/^{38}\text{Ar}_{\text{run}}$  vs  $^{40}\text{Ar}_{\text{tot}}/^{36}\text{Ar}_{\text{atm}}$  three-isotope ratio plot showing variations in the Ar isotopic signature for the different ablated FI in the Flysch Helminthoides and Schistes Lustrés units:**

(a). Three-isotope ratio plot showing variations of all the Schistes Lustrés samples. (b). Three-isotope ratio plot showing variations of all the Flysch Helminthoides samples. The different colours correspond to different samples from both units .

# SCHISTES LUSTRE



# FLYSCH HELMINTHOIDES

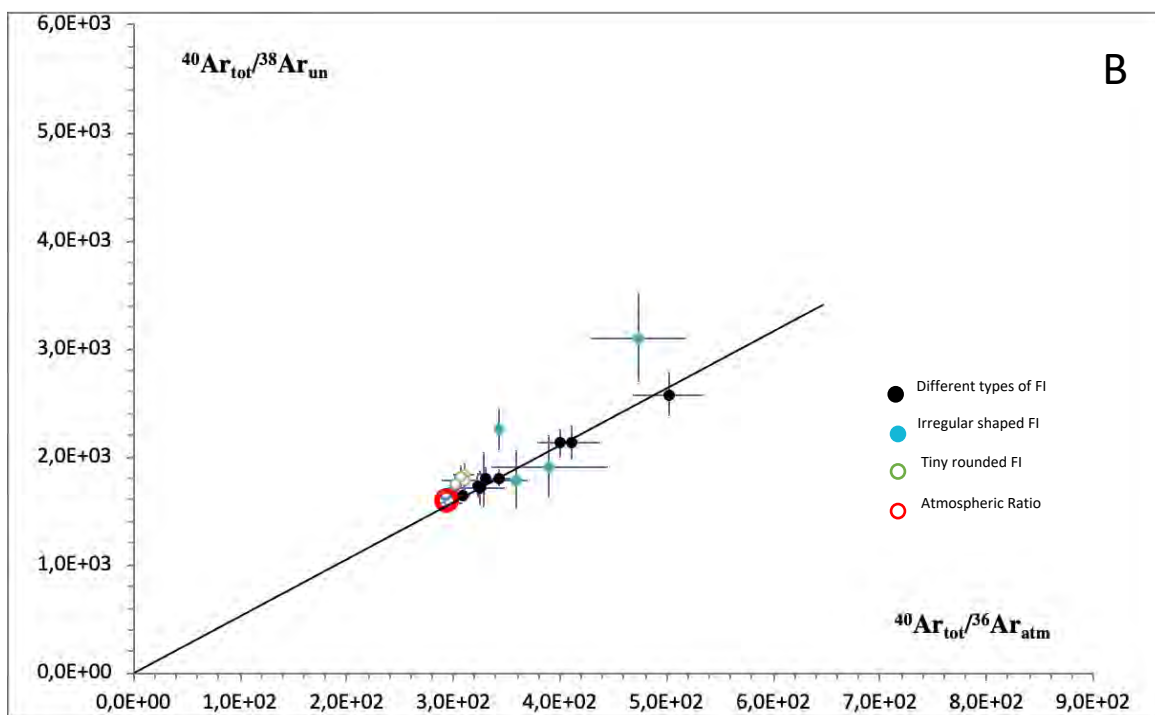


**Fig. 6.4:**  $^{40}\text{Ar}_{\text{tot}}/^{38}\text{Ar}_{\text{run}}$  vs  $^{40}\text{Ar}_{\text{tot}}/^{36}\text{Ar}_{\text{atm}}$  three-isotope ratio plot showing variations in the Ar isotopic signature for the different ablated FI in the Flysch Helminthoides and Schistes Lustrés units:

(a). Sample SL-15-14. Note huge variations recorded among the different FI's of each sample, the different point analyses scattering along an array trending away from the **atmospheric ratio (red dot)**. (b). Sample SL-FH114 shows a more clustered plot nearer to the atmospheric ratio. The data show that the samples have a non-atmospheric component contributing to the isotopic variation and that these isotopic variations are spatially tied to small-scale textural variations at the scale of the single FI's (i.e., < 100  $\mu\text{m}$ )

Table 6.1: Summary of the correlation of textural setting of fluid inclusions and there isotopic ratios

Sample	Types of Qz grains	Mineral inclusions	Decreepitated FI	Small Tiny FI	FI along subgrain-boundary	Trails of FI	$^{40}\text{Ar}_{\text{out}}$	$^{36}\text{Ar}_{\text{inn}}$	Isotopic values Average	Comments
SL-15-14	Large Qz + Recrystallized	+	+				1,160E-01	4,232E-04	High	Decreepitated FI associated with Car have higher isotopic ratio compare to other FI
SL-15-3B	Recrystallized		+	+	+		1,184E-01	4,495E-04	High	FI inclusions occurring together show higher isotopic ratio
SL-15-1	Recrystallized	+	+	+		+	3,450E-02	1,060E-04	High	Decreepitated FI associated with Car have higher isotopic ratio compare to other FI
SL-15-16	Recrystallized		+				2,476E-02	8,420E-05	High	Small size FI occurring together have higher isotopic ratio than the bigger FI occurring individually
SL-15-2	Large Qz grains	+	+	+			2,660E-02	7,918E-05	Low	Smaller decreepitated FI occurring together have higher $^{39}\text{Ar}_k$ isotopic values compared to the bigger FI
SL-15-4	Large Qz grains		+	+	+		1,158E-02	3,749E-05	Low	The FI inclusions align along the grain boundary have lower $^{39}\text{Ar}_k$ compared to the decreepitated FI
SL-15-13	Large Qz grains	+	+				4,016E-03	8,913E-06	Low	The big decreepitated FI have more $^{39}\text{Ar}_k$ and $^{36}\text{Ar}$ compared to tiny FI
FH4	Large Qz grains		+	+		+	8,863E-03	1,987E-05	Low	The irregular fluid inclusions and decreepitated fluid inclusions show higher $^{39}\text{Ar}_k$ compared to the fluid inclusions occurring as trails
FH13	Large Qz grains		+	+			4,755E-03	1,311E-05	Low	The single-phase fluid inclusion shows a high $^{39}\text{Ar}_k$ compared to the irregular bi-phase fluid inclusions
FH14	Large Qz + Recrystallized		+	+	+		4,310E-02	1,339E-04	High	The irregular shape decreepitated fluid inclusions show more abundance of $^{40}\text{Ar}_{\text{out}}$ and $^{36}\text{Ar}$ compared to the bi-phase fluid inclusions
FH2	Large Qz + Recrystallized		+	+			1,697E-02	4,962E-05	High	Decreepitated fluid inclusions show a higher $^{39}\text{Ar}_k$ compared to the tiny bi-phase fluid inclusions

FI: Fluid inclusions, Car: Carpholite mineral

## 7 Conclusion

This is the first study for texturally controlled in-situ UV laser ablation on fluid inclusions on the oceanic domains from the Western Alps in the two different units i.e. Schistes Lustre and Flysch Helminthoides. This study has tried to correlate Ar/Ar isotopic composition with typology of the different FI generations trapped in quartz minerals as a way to study the fluid fate during subduction and metamorphism. Some samples have (type-1) big quartz grains with lower abundances of fluid inclusions and some samples have (type-2) quartz grains that are recrystallized to an extent. It has been observed that the gas released from the fluid inclusions present in the highly recrystallized quartz grains have higher isotopic values ( $^{40}\text{Ar}_{\text{tot}}$  of  $4.706 \times 10^{-2}$ ; and  $^{36}\text{Ar}_{\text{atm}}$   $2.077 \times 10^{-4}$ ) compared to the fluid inclusions present in the bigger size quartz grains ( $^{40}\text{Ar}_{\text{tot}}$  of  $1.116 \times 10^{-2}$  and  $^{36}\text{Ar}_{\text{atm}}$   $3.171 \times 10^{-5}$ ).

The isotopic results show small-scale variation in isotopic values among the different types of fluid inclusions present in the samples. The  $^{40}\text{Ar}_{\text{tot}}/^{38}\text{Ar}_{\text{run}}$  vs  $^{40}\text{Ar}_{\text{tot}}/^{36}\text{Ar}_{\text{atm}}$  three-isotope correlation plot has been used to discriminate potential relationships between Ar reservoirs and hence different sources of the trapped fluids. We showed that the fluid inclusions having an isotopic ratio which lies on the theoretical trend plotted is a result of addition of  $^{40}\text{Ar}$  from the crustal rocks. The isotopic ratio that are isolated from this trend point to a third (and maybe more) component also contributing to the variations in isotopic ratio, the source of which is currently unknown.

However, the abundance of the  $^{39}\text{Ar}_K$  in all FI's is almost negligible indicating very low potassium concentration. This could provide an explanation of the apparent age calculated from the  $^{40}\text{Ar}/^{39}\text{Ar}$  data being unrealistically old ages with no geological significance, because the isotopic variations are dominated by the addition of unsupported  $^{40}\text{Ar}$  to the fluids, possibly coming from the degassing of a crustal component during the prograde Alpine cycle. We infer that the variation in the isotopic ratio obtained from the different types of fluid inclusions might reflect a difference in fluid source. The small-scale isotopic variation in fluid inclusions within the grains is clear that the fluid inclusions entrapment timing is different. In this study, the correlation that has been made with the textural setting of fluid inclusions and their isotopic composition should be a great value for better understanding of the fluid circulation regime in the different structural units along the subduction plate.

## 8 Acknowledgments

First and foremost I would like to take this opportunity to convey my sincere gratitude to my supervisors Dr. Stephane Sciallet, Dr. Raimbourg Hugues and Dr. Catherine Lerouge for their constant support and exemplary guidance throughout this work. This work would not have been completed without their assistance and advice which were entirely important in completing this thesis. Their remarks, encouragement and motivation throughout the learning process of this master thesis have made my experience in research more productive and stimulating. Secondly I would like to thank the research engineer Mr. Florian Duval and CDD engineer Mr. Angelo Montolese for assisting and guiding me with the experimental approach in the Ar-Ar Laboratory which have helped me to complete my work. I would also like to thank the Department of Geodynamics at ISTO for its facilities and for providing me an opportunity to pursue my studies. Thirdly, I would like to thank Head of the Master programme Dr. Alexandre Fournier, Head of the International master Dr. Nobuaki Fuji, my referent Dr. Samuel Angiboust and Dr. Laurie Barrie for their advices and constant help during my internship and studies at IPGP. I would also like to thank CNRS, Orleans and Referentiel Geologique de la France (RGF) for providing the research funding for this work.

Last but not the least, I would like to thank my family for their motivation at every step and my friends for their constant support and providing a rejuvenating social ambience during my stay here in Paris, making a home away from home.

## 9. References

Ph Agard, P Monié, L Jolivet, and B Goffé. Exhumation of the schistes lustrés complex: in situ laser probe  $^{40}\text{Ar}/^{39}\text{Ar}$  constraints and implications for the western alps. *Journal of metamorphic Geology*, 20(6):599–618, 2002.

Philippe Agard, B Goffé, Jacques LR Touret, and Olivier Vidal. Retrograde mineral and fluid evolution in high-pressure metapelites (schistes lustrés unit, western alps). *Contrib. Mineral. Petrol*, 140:296–315, 2000.

Philippe Agard, Laurent Jolivet, and Bruno Goffé. Tectonometamorphic evolution of the schistes lustrés complex; implications for the exhumation of hp and uhp rocks in the western alps. *Bulletin de la Société géologique de France*, 172(5):617–636, 2001.

Philippe Agard, Philippe Yamato, Laurent Jolivet, and Evgenii Burov. Exhumation of oceanic blueschists and eclogites in subduction zones: timing and mechanisms. *Earth-Science Reviews*, 92(1-2):53–79, 2009.

MICHEL BALLEVRE, Yves LAGABRIELLE, and OLIVIER MERLE. Tertiary ductile normal faulting as a consequence of lithospheric stacking in the western alps. *Mémoires de la Société géologique de France*, 156:227–236, 1990.

Gray E Bebout, Philippe Agard, Katsura Kobayashi, Takuya Moriguti, and Eizo Nakamura. Devolatilization history and trace element mobility in deeply subducted sedimentary rocks: Evidence from western alps hp/uhp suites. *Chemical Geology*, 342:1–20, 2013.

Mathieu Bellanger, Romain Augier, Nicolas Bellahsen, Laurent Jolivet, Patrick Monié, Thierry Baudin, and Olivier Beyssac. Shortening of the european dauphinois margin (oisans massif, western alps): New insights from rscm maximum temperature estimates and  $^{40}\text{Ar}/^{39}\text{Ar}$  in situ dating. *Journal of Geodynamics*, 83:37–64, 2015.

S Bogdanoff. Evolution de la partie occidentale du massif cristallin externe de l'argentera. place dans l'arc alpin. *Géol. France*, 4:433–453, 1986.

Jean-Michel Caron. Lithostratigraphie et tectonique des Schistes lustrés dans les Alpes cottiennes septentrionales et en Corse orientale.

Ch Chopin. Magnesiochloritoid and magnesiochloritoid; two index minerals of pelitic blueschists and their preliminary phase relations in the model system  $\text{MgO-Al}_2\text{O}_3\text{-SiO}_2\text{-H}_2\text{O}$ . *American Journal of Science*, 283:72–96, 1983.

MA Kendrick, R Duncan, and D Phillips. Noble gas and halogen constraints on mineralizing fluids of metamorphic versus surficial origin: Mt Isa, Australia. *Chemical Geology*, 235(3-4): 325–351, 2006.

MA Kendrick, G Mark, and D Phillips. Mid-crustal fluid mixing in a proterozoic Fe oxide–Cu–Au deposit, Ernest Henry, Australia: evidence from Ar, Kr, Xe, Cl, Br, and I. *Earth and Planetary Science Letters*, 256(3-4):328–343, 2007.

C Kerckhove. Schéma structural de la nappe du flysch helminthoïdes de l'aembrunais-ubaye. Trav. Lab. Geol. Fac. Sci. Grenoble, 39:7–24, 1963.

C Kerckhove, M Gidon, and JL Pairis. Carte géologique de la France (1/50000) feuille embrun-guillestre (2<sup>e</sup> édition, coupure spéciale)(871): Orléans. Bureau de Recherches Géologiques et Minières, 2005.

Claude Kerckhove. La zone du flysch dans les nappes de l'aembrunais-ubaye (alpes occidentales). Géologie alpine, 45:5–204, 1969.

O Merle and JP Brun. La déformation polyphasée de la nappe du parpaillon (flysch à helminthoïdes): Un résultat de la déformation progressive associée à une translation non rectiligne. CR Acad. Sci, 292:343–346, 1981.

Geoffroy Mohn, Gianreto Manatschal, Othmar Müntener, Marco Beltrando, and Emmanuel Masini. Unravelling the interaction between tectonic and sedimentary processes during lithospheric thinning in the alpine tethys margins. International Journal of Earth Sciences, 99(1): 75–101, 2010.

Simon A Peacock. Fluid processes in subduction zones. Science, 248(4953):329–337, 1990.

Pascal Philippot. Fluid-melt-rock interaction in mafic eclogites and coesite-bearing metasediments: constraints on volatile recycling during subduction. Chemical Geology, 108(1-4): 93–112, 1993.

Fabrizio Piana, Alessia Musso, Carlo Bertok, Anna d'Atri, Luca Martire, Elena Perotti, Dario Varrone, and Giorgio Martinotti. New data on post-eocene tectonic evolution of the external ligurian Briançonnais (western ligurian alps). Italian Journal of Geosciences, 128(2):353–366, 2009.

Hugues Raimbourg, Maxime Vacelet, Claire Ramboz, Vincent Famin, Romain Augier, Giulia Palazzin, Asuka Yamaguchi, and Gaku Kimura. Fluid circulation in the depths of accretionary prisms: an example of the Shimanto belt, Kyushu, Japan. Tectonophysics, 655:161–176, 2015.

Hugues Raimbourg, Vincent Famin, Giulia Palazzin, Mathieu Mayoux, Laurent Jolivet, Claire Ramboz, and Asuka Yamaguchi. Fluid properties and dynamics along the seismogenic plate interface. Geosphere, 14(2):469–491, 2018.

Edwin Roedder. Volume 12: Fluid inclusions. Mineralogical Society of America, 1984.  
Marco Scambelluri and Pascal Philippot. Deep fluids in subduction zones. Lithos, 55(1-4):

213–227, 2001.

Asuka Yamaguchi, Kohtaro Ujiie, Shun'ichi Nakai, and Gaku Kimura. Sources and physicochemical characteristics of fluids along a subduction-zone megathrust: A geochemical approach using syn-tectonic mineral veins in the Mugai mélange, Shimanto accretionary complex. Geochemistry, Geophysics, Geosystems, 13(7), 2012.